9-20-2012

Investigation of bolometric and resistive properties of nickel oxide

Shaurya Kumar

Investigation of Bolometric and Resistive Properties of Nickel Oxide

By

Shaurya V. Kumar

A thesis submitted in partial fulfillment of the requirements for the degree of
Master of Science in Material Science and Engineering

Center for Material Science & Engineering
College of Science
Rochester Institute of Technology
Rochester, New York
September 20, 2012

Committee Approval:

Dr. Lynn F. Fuller (Thesis Advisor)	_____	Date: _____
Dr. Santosh K. Kurinec (Committee Member)	_____	Date: _____
Dr. Michael A. Jackson (Committee Member)	_____	Date: _____
Dr. Jacob Noel-Storr (Committee Member)	_____	Date: _____
Dr. Kalathur Santhanam (Program Director)	_____	Date: _____

I dedicate this thesis to my loving family: my father Virender, my mother Neeta, and my brother Angad. Your constant support, encouragement and guidance throughout my life have allowed me to complete my education. Words cannot express the gratitude and appreciation that I feel for all that you have done for me.

Acknowledgements

I would like to acknowledge my thesis committee advisor Dr. Fuller who allowed me great flexibility in choosing the direction of this work. I would also like to acknowledge my committee members Dr. Kurinec, Dr. Jackson, and Dr. Noel-Storr. Thank you all for finding the time in your busy schedules to assist and guide me in my research.

I would also like to thank the entire faculty of the Department of Electrical and Microelectronic Engineering and Center for Material Science & Engineering for educating me over the course of my time here at the institute, both as an undergraduate as well as a graduate student. I would also like to thank Dr. Kurinec, for playing a key role in starting the BS Microelectronic Engineering, MS Material Science and Engineering dual degree, thereby providing me this unique opportunity to learn from two different, yet closely-related colleges.

I would also like to thank Dr. Michael Pierce from the College of Science at Rochester Institute of Technology, and his student Siddharth Gopal, for providing the XRD results and analyses used in this study. I would also like to thank the Failure Analysis team at Micron Technology Inc., specifically Dr. David MacMahon and Claudia Sotomayor, for providing the TEM and EDS analysis used in this study.

The entire staff of the RIT Semiconductor and Microsystems Fabrication Laboratory is thanked for their continuous equipment and project support throughout the years, and allowing me to gain familiarity with the facility by working there as a student technician

in my early years at the institute. I would like to specifically thank the following staff members: Thomas Grimsley for enforcing the safety regulations in the lab, and providing mask making facilities to students; Scott Blondell for maintaining the facility, and hiring me as a student technician; John Nash on several occasions where he spent time training and troubleshooting for several tools; Richard Battaglia for troubleshooting for the LAM 490 plasma etcher, CVC 601 sputterer, and GaSonics Asher; Dave Yackoff for helping create the nickel oxidation furnace recipe on Bruce Tube 8; Bruce Tolleson for frequent troubleshooting on the SSI wafertrack and training for the DryTek Quad etcher; and finally Sean O'Brien who has always made himself available to the students both for tool training and troubleshooting, as well as project assistance. I would also like to thank Dan Smith and David Cabrera, both graduate students enrolled in the microelectronic engineering program, for help with sample preparation and electrical testing respectively.

Most importantly, I would like to thank my entire family for their support. All of you have been a huge part of my life and have made me the person I am today. Additionally, I would like to thank my cousin Ravnish Luthra and Uncle Sunil Verma for providing timely financial support for my education, which has allowed me to pursue this Master's Degree. I would like to thank my cousin Jivan, who I consider my older brother, for providing me with not just timely support and advice, but also some great laughs and great times. I would also like to thank my brothers from Phi Kappa Psi fraternity, New York Theta chapter who kept me motivated and helped build my character. I am lucky to have so many people who genuinely care about me and take such great interest in my life. I thank you all with utmost gratitude in my heart.

Abstract

This work investigates the properties of nickel oxide for use in microbolometric and resistive memory applications. For the uncooled infrared radiation detector industry, the current standard sensor materials are either very expensive, but very sensitive (vanadium oxide), or the other extreme of low cost, and low quality (amorphous silicon). Thus, a need arises for a medium-grade, medium-cost microbolometer sensitive material. The physical scaling limits of conventional charge-based non-volatile memory has progressed the semiconductor industry into searching for a new type of non-volatile memory device. Resistive random access memory (ReRAM) shows promise to fill this void, and nickel oxide presents itself as a potential forerunner in this market by demonstrating its ability to switch from a high resistance state to a low resistance state.

A die with microbolometer devices and metal-insulator-metal (MIM) structures was designed and fabricated, with nickel oxide as the infrared-sensitive and resistance-switching material respectively. Two methods of obtaining nickel oxide were investigated – plasma oxidation and thermal oxidation. Ellipsometry, X-ray diffraction, transmission electron microscopy, and energy dispersive X-ray spectroscopy were used to study the films created using the two techniques. Thermally grown nickel oxide was used for the fabrication of the bolometer and MIM devices, which were subsequently electrically tested to observe their performance and evaluate the viability of nickel oxide for use in these applications. Thermal nickel oxide successfully demonstrated its viability for both applications.

Table of Contents

List of Figures

List of Tables

Chapter 1

Introduction and Motivation

Nickel oxide is a very versatile material. It has been found to be useful in Nickel metal halide (NiMH) batteries, chemical sensors, electrodes in fuel cells, as an antiferromagnetic material, and as an electrochromic material to name a few. [1] Recently, nickel oxide has been discovered as a viable detector material for microbolometer and resistive memory applications, thus warranting study of its bolometric and resistive properties.

1.1 Nickel oxide for use in microbolometric applications

A microbolometer is an infrared sensitive resistor whose resistance changes depending on incident infrared radiation. Since all materials emit infrared radiation based on their temperature (blackbody radiation), this kind of sensor can be used for thermal imaging and sensing applications.

At present, uncooled infrared radiation detectors have competitive price and infrared sensitivity due to the gradual development of MEMS and integrated circuit technology. For the purpose of maximizing the infrared radiation detector performance in an uncooled detector, the characteristics of the microbolometric materials that exist on the membrane of the MEMS structure, such as the morphology, resistance change due to temperature, noise characteristics, and other factors, should be considered.

Crystalline nickel oxide (NiO) demonstrates high resistivity by having very few carriers and low mobility of those carriers. A NiO film having a resistivity of about 0.1Ωcm can prove to be a good candidate as a microbolometric material. Traditional infrared-sensitive microbolometric materials that have been widely studied include vanadium oxide (VO_x), and amorphous silicon (a-Si). Currently, VO_x and a-Si demonstrate a temperature coefficient of resistance (TCR) value of slightly higher than 2%/°C, thereby becoming the two most widely used materials. NiO is demonstrated as a feasible material for microbolometric applications by comparing the merits and demerits of it versus VO_x and a-Si. [2]

There are several reasons why nickel oxide is potential candidate material for microbolometer applications. First, the high resistivity (~10^{13} Ω cm) of stoichiometric NiO can be reduced depending on film growth mechanism resulting in non-stoichiometry making the film applicable for an uncooled infrared detector. Second, the growing of the NiO film and device fabrication process is fully compatible with existing CMOS processes, whereas VO_x is not. Third, the simple fabrication process and availability of low price materials makes it a very appealing material. The fourth advantage is that nickel oxide only exists in two possible phases: nickel (II) oxide (NiO) and nickel (III) oxide (Ni_2O_3), thus providing reproducibility and long term stability, along with low noise characteristics. [1]

1.2 Nickel oxide for use in resistive memory applications

The physical scaling limits of conventional charge-based non-volatile memory have pressed the semiconductor industry into searching for a new type of non-volatile memory device. Resistive random access memory (RRAM or ReRAM), that can be repeatedly switched between a high and a low resistance value by an applied voltage pulse, is one of desirable concepts and recently attracted a great deal of scientific and technological interest. [3] These repeatable behaviors of resistance switching had been observed in a lot of insulating systems, especially binary transition metal oxides such as NiO. Since the switching characteristics of dielectric NiO_x thin film was discovered by Gibbons and Beadle [4], NiO_x is particularly attractive for non-volatile memory device due to its high-speed and low power switching characteristics. The mechanism of the switching behavior, which, despite immense research efforts, has not been fully understood and still leaves unanswered questions, is largely related to a repeating thermo-chemical mechanism of formation and subsequent rupturing due to Joule heating of low resistance conduction paths [5] [6], often referred to as filaments, as shown in Figure 1.1.

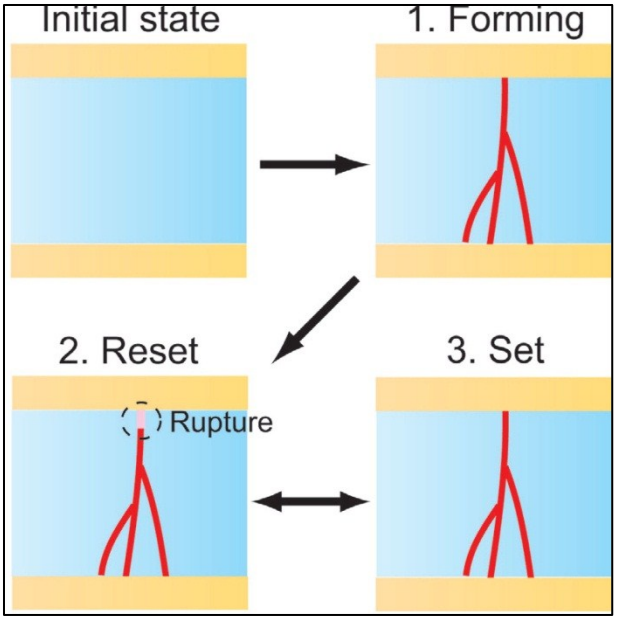

Figure 1.1: Formation and rupture (set and reset) of conducting filaments. [3]

The following chapters of this thesis discuss the investigation of the viability of nickel oxide for use in microbolometric and resistive memory applications. Chapter 2 provides some background on the microbolometers and resistive memory concepts, nickel oxidation mechanism, along with a description of the various film deposition/growth processes and analysis techniques employed. Chapter 3 presents the layout and design of the sensor, along with a detailed description of the fabrication process. Chapter 4 discusses the results obtained from the various analyses, leading to a conclusion and recommendations for future work in Chapter 5.

Chapter 2

Background

2.1 Microbolometers

Microbolometers were first developed by Honeywell International, Inc. in the late 1970s as a classified contract for the United States Department of Defense. The technology was later declassified in 1992 and was licensed to different manufacturers.

The microbolometer is a resistive element constructed with a detector material with a very small thermal capacity and large temperature coefficient of resistance so that the absorbed infrared radiation produces a large change in electrical resistance. All materials at a temperature above absolute zero emit a particular wavelength of infrared light as blackbody radiation. This incoming radiation into the detector produces heat within the detector material, which in turn produces the electrical resistance change. There is no direct photon-electron interaction involved. This sensitivity to temperature of a material is known as its temperature coefficient of resistance (TCR), usually denoted in %/°C. The change in resistance can be measured and converted to temperature readings after calibration.

2.1.1 Advantages and disadvantages of microbolometers

When comparing different types of thermal imagers, microbolometers have distinct advantages and disadvantages. Microbolometers, unlike most other thermal imagers, do not require cooling and are hence often referred to as uncooled thermal imagers. This results in a less complicated and cheaper design of the sensor. Microbolometers typically absorb best in the wavelength range of 7.5 μm to 14 μm in the electromagnetic spectrum, which provides the best penetration through smoke, dust, etc. thereby making it perfect for most thermal imaging applications. They also typically consume much less power than other types of imagers, and also have a longer lifetime. [1]

However, microbolometers are less sensitive than other imagers, and are not usually used for high definition imaging applications, but rather for Boolean sensing applications. They also cannot be used for multispectral or high-speed infrared applications. This limits the applicability of a particular microbolometer imager to different applications, but a particular microbolometer can be optimized for specific applications.

Development efforts in the microbolometer industry are now going in two directions:

1. Microbolometer arrays for high sensitivity applications such as military, space, and other high-end commercial applications.

2. Microbolometer arrays for commercial applications with the lowest possible cost.

The key factor is to obtain a high performance sensor together with high thermal isolation in the smallest possible area.

2.1.2 Factors involved in choosing a microbolometer detector material

There are four major properties to consider when choosing an infrared sensitive material:

- Temperature coefficient of resistance (TCR)
- CMOS compatibility
- Stoichiometric reproducibility
- Noise

To obtain a highly sensitive microbolometer, the TCR must be maximized. Obviously, the CMOS compatibility and the stoichiometric reproducibility of the film must also be maximized. However, the noise behavior of the film must be minimized to obtain a high signal-to-noise ratio – a useful signal.

Conventional microbolometric materials include vanadium oxide (VO_x), amorphous silicon (a-Si), and many others. Nickel oxide (NiO) is investigated for use as a viable microbolometric infrared-absorptive material. Table 2.1 below shows a comparison of the four important properties (as mentioned above) of these three materials.

Table 2.1: Comparison of Microbolometric Properties [1,2,7,8]

Material	TCR (%/°C)	Noise	Reproducibility	CMOS Compatibility
VO_x	2	Low	Bad	Bad
a-Si	2	High	Good	Good
NiO	-3.3	Feasible	Good	Good

Nickel oxide was recently discovered as a viable microbolometric material and has therefore not been integrated into the mainstream microbolometer industry. Current leaders are vanadium oxide that allows for high-sensitivity (and high cost) thermal imaging, and amorphous silicon, which provides for lost-cost, low-sensitivity imaging. Nickel oxide can bridge this gap with cheap, relatively good sensitivity imagers.

2.1.3 Temperature Coefficient of Resistance

The most important figure of merit when comparing different materials for microbolometric applications is the temperature coefficient of resistance. This is usually expressed as a percentage change per degree Celsius, and can be calculated as shown in Eq. 2.1.

$$TCR = \alpha = \frac{1}{R_o}\frac{\Delta R}{\Delta T}\% \qquad \textbf{Eq. 2.1}$$

where R_o is the default resistance prior to exposure to incoming infrared radiation. When a fixed current I is applied to this microbolometer, the change in voltage can be expressed as shown in Eq. 2.2.

$$\Delta V = I\Delta R = IR\alpha\Delta T \qquad \textbf{Eq. 2.2}$$

Conversely, a fixed voltage V will result in a change of current as shown in Eq. 2.3

$$\Delta I = \frac{V}{\Delta R} = \frac{V}{R\alpha\Delta T} \qquad \textbf{Eq. 2.3}$$

2.2 Resistive Memory

Since the early 1960s, there has been increasing interest in the conductivity in metal-insulator-metal (MIM) structures, and various electrical conduction phenomena including resistive switching and its application to resistive memory devices. This interest is fueled by the need for higher performance non-volatile memory for the ultra-high speed broadband era. Flash memory is one of the current most major forms of non-volatile memory and its density is expected to be continuously increased, until the physical limit for minimum feature size has been reached. [9]

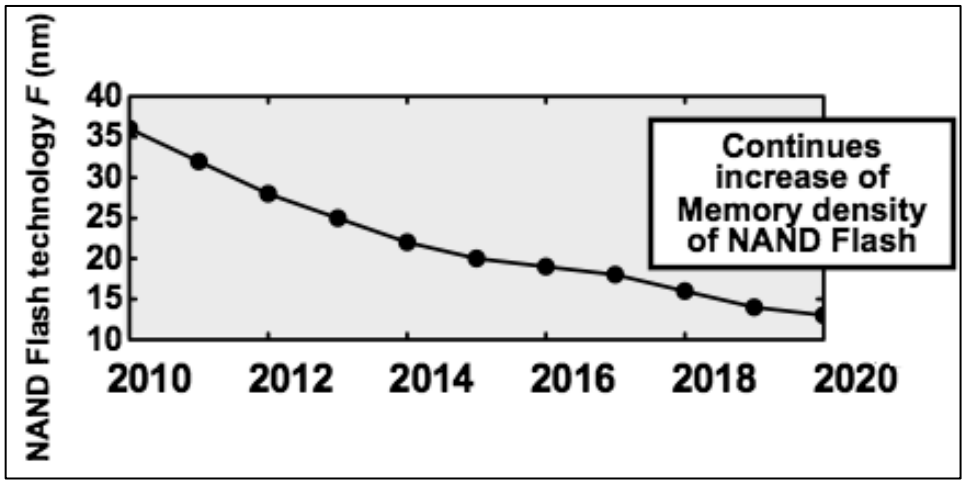

Figure 2.1: Continuous decrease of Flash memory feature size, increasing density [9]

As the physical limit approaches, the need for a new form of non-volatile memory becomes crucial, especially one that provides the following traits [9]:

- Data non-volatility
- Low power operation
- High speed operation
- High cycle endurance

Resistive random access memory (RRAM) shows promise in all these traits and is a strong contender for being the leader in non-volatile memory applications in the next few decades.

2.2.1 Resistive memory operation kinetics

Despite its early discovery in the 1960s the physics of the resistive memory switching are still not fully understood. Many models have been proposed to explain the resistive switching behavior observed in transition metal oxide materials such as filamentary conduction mechanisms, charge trapping defects states inside the band gap, trap-controlled space-charge-limited current, and charge trap states at metal/oxide interfaces with a change of a Schottky-like barrier. [6] It is also not yet clear if these effects take place in the bulk of the material or in confined regions close to the electrodes. [10] The exact origin of a particular material's resistive switching mechanism is defined by its own material properties, and there is no current globally applicable theory for explaining

resistive switching in any material. To test the switching behavior of a particular material, a simple metal-insulator-metal (MIM) capacitor can be constructed, where the insulator, in this case, is NiO. The electrical behavior of this device is then observed when stimuli such as voltage bias across the device, constant current bias through the device, length of time of measurement, voltage pulses, heat, etc. are applied.

Most literature sources [2,6,11] cite formation of filamentary conduction paths and their subsequent rupture due to a non-negligible Joule heating effect as the mechanism of resistive switching observed in NiO.

2.3 Nickel and Nickel Oxide Properties

2.3.1 Nickel Metal

Nickel (chemical symbol Ni) was first discovered by Saxon miners over 2000 years ago, as a reddish-colored ore, NiAs, which superficially resembled Cu_2O. The miners attributed their inability to extract copper from this compound to the work of the devil, and named the ore "Kupfernickel" (Old Nick's Copper). Later on, in 1751, a Swedish mineralogist Axel Fredrik Cronstedt was able to successfully extract a relatively impure metal from the ore, subsequently naming "Nickel". Its physical and chemical properties were more accurately understood only over 50 years later by the German chemist, J. B. Richter. [12]

Today, almost 250 years after its discovery, nickel is reasonably well known and understood, and its practical applications are abundant; yet it continues to amaze the scientific community with new practical applications. Nickel is the seventh most abundant transition metal element, and the 22^{nd} most abundant element in the Earth's crust – about 99 ppm [12], although it is rarely found in its elemental form, usually in an alloy form with iron. An iron-nickel mixture is thought to compose the Earth's core. [13]

Pure nickel is lustrous, silvery-white metal, with a slight golden tinge. A nickel sputter target is shown in Figure 2.2. It is hard and ductile, and shows significant top-surface reactivity even in room temperature conditions in air, forming a thin passive layer of nickel oxide that prevents further oxidation. Nickel is therefore, largely considered

corrosion-resistant and is therefore used for electroplating metals such as brass and iron. However, at higher temperatures, further oxidation of nickel is possible to form thicker films of nickel oxide.

Figure 2.2: Nickel Sputter Target [14]

Nickel is one of the four elements that are ferromagnetic around room temperature, the other three being iron, cobalt, and gadolinium. It is therefore commonly used to form medium-strength permanent magnets such as Alnico magnets. Nickel is most popular for its use in alloys; about 60% of the world's production of nickel is used for forming nickel-steels like stainless steel. Nickel is often used in the semiconductor industry, especially beyond the 65 nm node, for forming nickel silicides (NiSi) that aid in low resistivity ohmic contact formation, such as between a metal electrode and the silicon surface.

Nickel has an atomic number of 28, and has 5 known naturally occurring isotopes (^{58}Ni, ^{60}Ni, ^{61}Ni, ^{62}Ni, and ^{64}Ni). The atomic weight of nickel is 58.69 g/mol and electronegativity of 1.91 on the Pauling scale. The unit cell of nickel is a face-centered cube (FCC) with the lattice parameter of 3.524 Å giving an atomic radius of 1.24 Å. Its electron configuration is $[Ar]3d^8 4s^2$. Its density near room temperature is about 8.91 g/cm^3. Solid nickel melts at 1455 °C and subsequently boils at 2913 °C. Its electrical resistivity in its pure metal form is 6.93 μΩ*cm at 20 °C. [15,16]

2.3.2 Nickel Oxide

Nickel oxide, specifically, nickel (II) oxide (NiO), is a very well characterized oxide of nickel, and is classified as a basic binary transition metal oxide. NiO adopts the cubic NaCl structure, sometimes called the rock salt structure, with octahedral Ni(II) and O^{2-} sites and lattice parameter of 4.178 Å. [17] Like most other binary metal oxides, NiO is often non-stoichiometric, meaning that the Ni:O ratio deviates from 1:1. When produced in a good stoichiometric ratio, nickel oxide is greenish-yellow in color. Grey or black nickel oxides are indicative of nonstoichiometry.

The molar mass of NiO is 74.69 g/mol, and its density in solid form is 6.67 g/cm^3. [16] Nickel oxide melts at 1955 °C, and solid nickel oxide is not soluble in water. [18] Its optical properties vary based on film thickness and synthesis technique, but it is generally opaque to visible light, but absorptive in the infrared range of the electromagnetic spectrum, thereby making it apt for bolometric applications.

2.3.2.1 Nickel Oxidation Kinetics

Nickel forms a passive oxide film on the surface in room temperature which protects the underlying nickel bulk from further oxidation. Its Pilling-Bedworth ratio (P-B ratio) is calculated as shown by Eq. 2.4.

$$P-B\ Ratio = \frac{1}{n}\frac{A_O}{A_M}\frac{d_M}{d_O} = \frac{1}{1}\frac{74.69\,g/mol}{58.69\,g/mol}\frac{8.91\,g/cm^3}{6.67\,g/cm^3} = 1.7 \qquad \textbf{Eq. 2.4}$$

where n is the number of metal atoms in the oxide, A_O is the molar mass of the oxide, A_M is the atomic weight of the metal, d_M is the density of the metal, and d_O is the density of the oxide. An ideal protective passive oxide film would have a P-B ratio of exactly 1.0. A P-B ratio less than 1.0 indicates a nonprotective, porous film. [19] A P-B ratio greater than 1.0 indicates a protective film with compressive stress on the underlying metal. At P-B ratios great than 2, these stresses cause the oxide film to crack. With a P-B ratio of 1.7, the top surface NiO film protects the underlying Ni with some compressive non-negligible stress.

At higher temperatures (>400 °C), this stress causes the nickel oxide film to break down and allows for further oxidation of nickel. This oxidation is governed by the parabolic growth model as shown in Eq. 2.5.

$$\frac{dy(t,T)}{dt} = \frac{k(T)}{y(t,T)} \qquad \textbf{Eq. 2.5}$$

where y is the oxide thickness, t is time, and k is the reaction rate constant, given by Eyring's equation in Arrhenius form as shown in Eq. 2.6.

$$k(T) = \frac{k_B T}{h} \exp\left(-\frac{\Delta H - T\Delta S}{RT}\right) \qquad \textbf{Eq. 2.6}$$

where k_B is the Boltzmann's constant, T is the absolute temperature in Kelvins, h is Planck's constant, ΔH is enthalpy of activation, ΔS is the entropy of activation, and R is the gas constant. Eq. 2.6 is a first-order nonlinear ordinary differential equation, and can be solved to obtain Eq. 2.7.

$$\left[y(t,T)\right]^2 = 2k(T)t + y_0^2 \qquad \textbf{Eq. 2.7}$$

$$\Delta y(t,T) = y(t,T) - y_0 \qquad \textbf{Eq. 2.8}$$

where y_0 is the oxide thickness at $t = 0$. If $\Delta y(t,T)$ is defined as shown in Eq. 2.8, then Eq. 2.7 can be further expressed as shown in Eq. 2.9.

$$\Delta y(t,T) = \left(\frac{2k(T)t}{\Delta y(t,T)}\right) - 2y_0 \qquad \textbf{Eq. 2.9}$$

Substituting Eq. 2.6 in Eq. 2.9, an expression for film thickness growth as a function of time and absolute temperature is obtained as shown in Eq. 2.10.

$$\Delta y(t,T) = \left(2\frac{k_B T t}{h\Delta y(t,T)} \exp\left(-\frac{\Delta H - T\Delta S}{RT}\right)\right) - 2y_0 \qquad \textbf{Eq. 2.10}$$

The values for the enthalpy of activation and entropy of activation for nickel oxidation have been tabulated by Moore and Lee, as shown in Table 2.2.

Table 2.2: Tabulated Values for Enthalpy and Entropy of Formation for Nickel Oxidation [20]

Parameter	Definition	Value
ΔH	Enthalpy of activation	34.7 ± 0.8 kcal
ΔS	Entropy of activation	-17.3 ± 0.9 cal/deg

2.4 Film Deposition/Growth Techniques Employed

Various film deposition techniques were used to deposit the different films necessary for the fabrication of the devices. These films were deposited at the RIT Semiconductor and Microsystems Fabrication Laboratory (SMFL).

2.4.1 Photoresist Coating

Photoresist coating and development of 6" substrates was conducted on the SSI track.

Figure 2.3: SSI Track [21]

A photoresist is made up of three main components. The first component is a base matrix that holds the photoresist together and attributes to adhesion and film forming abilities with the addition of etch resistance. The second component is the photosensitizer that causes a chemical reaction with the absorbance of the photons it is irradiated with, which

in turn, makes the resist more soluble in an alkaline solution. The third component is the solvent that makes the resist viscous. The majority of the solvent evaporates after application during spin-coat process. In this project, the Fujifilm OiR 620M positive photoresist is used. Its base matrix resin is novolac, and its photosensitizer is DNQ (Diazonapthoquinone).

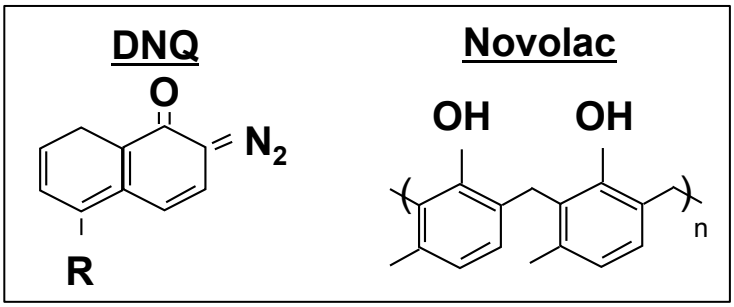

Figure 2.4: DNQ and Novolac Compounds

There are various steps involved in the coating and development processes respectively. The wafers are first vapor-primed with HMDS (Hexamethyldisalizane) after a dehydration bake (140 °C for 60 seconds). HMDS is an organic, flammable solvent and is used to treat substrate surfaces prior to photoresist coating. When an organic photoresist with a high surface tension is coated over a hydrophilic, low surface tension surface (such as silicon dioxide), dewetting and adhesion problems can occur. Exposure of the low surface tension substrate surface with HMDS will chemically convert the surface to raise its surface tension to match the organic photoresist. Over exposure to the HMDS can also result in adhesion problems; in the automatic SSI track, it is used in full strength. [21] The purpose of the dehydration bake is to reduce the level of water

molecules from the wafer surface. Baking in a convection oven for 20 minutes is equivalent to baking on a hotplate for 1 minute.

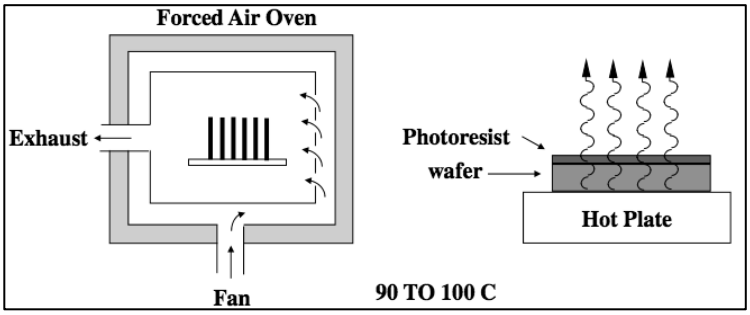

Figure 2.5: Dehydration Bake Techniques [22]

After the dehydration bake, and a brief wafer cooling step, the wafer is loaded into the photoresist dispense module. Here, the robot dispenses a fixed amount (depending on the recipe) of Fujifilm OiR-620M positive photoresist. This is a type of i-line photoresist, and is therefore most sensitive to i-line (365 nm wavelength) radiation. The wafer is then spun at 3250 rpm for 30 seconds, followed by a softbake (90 °C for 30 seconds). The softbake must not be at too high of a temperature as that risks destroying the photoactive compound – in this case DNQ (Diazonapthoquinone). The purpose of the softbake is to reduce the amount of solvent in the photoresist film from around 20 – 30% down to 4 - 7%. This spin speed defines the end resulting resist thickness and uniformity. For the standard coat recipe, a spin speed of 3250 rpm provides a ~1 μm thick uniform photoresist film.

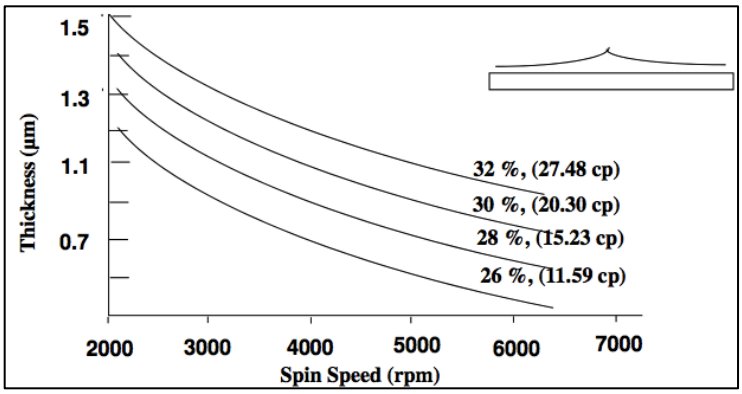

Figure 2.6: Tabulated Resist Thickness vs. Spin Speed [22]

2.4.2 Photoresist Exposure and Development

Photoresist exposure is the process of irradiating the photoresist through a mask to create a pattern on the wafer. Photoresists are classified into two major types – positive and negative. Positive photoresists become more soluble in areas where they have been exposed, whereas negative photoresists become insoluble in areas where they have been exposed. In this case, the ASML PAS 5500/200 i-line 5x stepper is used to expose the OiR 620 positive photoresist. A mercury vapor radiation source emitting light of wavelength 365 nm is used on this ASML stepper.

During the exposure step, the DNQ undergoes photodecompostion to form a keto-carbene and nitrogen gas. This keto-carbene is short-lived and undergoes Wolff rearrangement leading to a ketene that reacts with water in the air to form a carboxylic acid which is the end base-soluble product. Figure 2.7 shows this entire photoreaction.

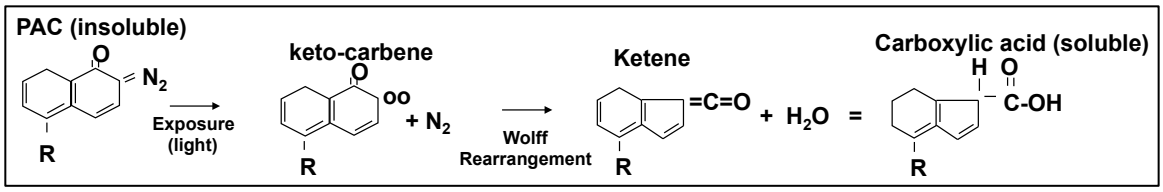

Figure 2.7: Photoreaction of DNQ

Photoresist development involves the wet removal of photoresist from undesirable areas (after exposure) to leave behind a pattern which masks the desired areas from a subsequent process, such as an etch step.

The first step in photoresist development is a post-exposure bake (PEB) step. This bake serves to reduce the amount of standing waves in the resist film. Standing waves are produced when coherent monochromatic light reflected back from a substrate interfere with incident light. The levels of constructive and destructive interference cause corresponding variations in the exposed sensitizer concentration in positive photoresist films. Minima or nulls occur at regular intervals calculated as shown in Eq. 2.11:

$$X = (2k+1)\frac{\lambda}{4n} \qquad \textbf{Eq. 2.11}$$

where λ is the exposure wavelength, n is the refractive index of the photoresist, and k is an integer. This kind of "scalloped" pattern and irregular photoresist thickness over topography can cause severe linewidth control problems. The post-exposure bake causes the unexposed sensitizer to diffuse from high concentration areas to low concentration areas. As the photoresist is taken above its glass transition temperature, the sensitizer

becomes somewhat mobile and tends to diffuse to eliminate the concentration gradient caused by the standing waves. In the standard develop recipe used on the SSI track, the PEB is done at 110 °C for 60 seconds.

Following a brief cooling step after the PEB, the wafer is transported into the developer module. Here, the robot dispenses a 50 second puddle of CD-26 developer, which is a TMAH (Tetramethylammoniumhydroxide) based alkaline developer. It reacts with the exposed portions of the photoresist film, which have become more acidic as part of the exposure to i-line radiation, and washes those areas away in the subsequent 30 second DI water rinse at 3750 rpm. The wafer is then spun dry. The last step in this process is a hard bake, which is done at or slightly above the glass transition temperature of the photoresist. In this project, the standard develop recipe employs the hard bake at 140 °C for 60 seconds. The resist is cross-linked, and thus toughened prior to plasma etch, pinholes are filled, and adhesion is improved. [22] No resist flow occurs at the substrate during this step, but rather during the bulk of the film as shown in Figure 2.8.

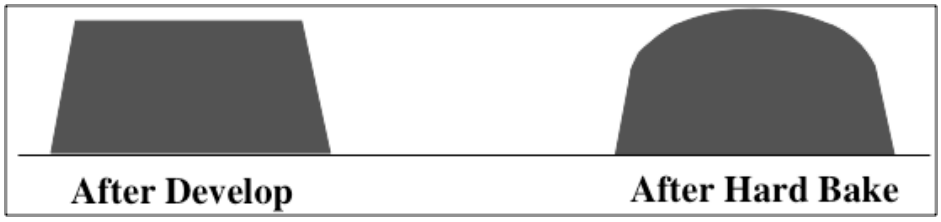

Figure 2.8: Resist Profiles Before and After Hard Bake [22]

2.4.3 DC Sputtering

Sputtering is a physical vapor deposition (PVD) process and usually takes place under vacuum. The vacuum pressure depends on process limitations and film purity requirements. Sputtering involves bombarding a target with high-energy ions. In conventional sputtering systems, these ions are formed from argon and/or nitrogen gas glow discharge. The target in the system is a solid disc that serves as the source of the deposition material. The target is electrically grounded while the gas is introduced into the chamber and is ionized to a positive charge.

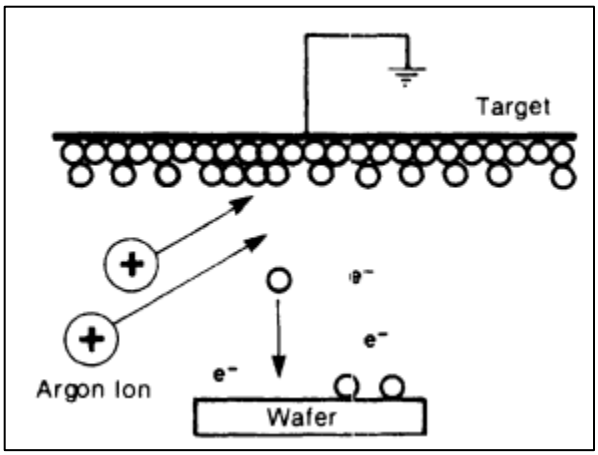

Figure 2.9: Physics of Sputtering [23]

Coulombic forces accelerate these positively charge ions to the grounded target. As they accelerate towards the target, their momentum steadily increases until they finally smash into the target. When these charged ions hit the target, their momentum is transferred into the atoms of the target material in the form of heat and lattice damage, which causes them get dislodged from the target and ejected into the chamber. These displaced target atoms

disperse throughout the entire chamber with some depositing onto the wafer(s) in the chamber. Film characteristics can be easily controlled in a sputtering process by adjusting the deposition parameters such as process pressure, power, and temperature of the substrate. A higher power increases the sputter rate, but can also lead to implantation, target overheating, and defectivity. Lower operating pressures increase film purity and mean-free path of dislodged target atoms, but achieving a very low pressure can take a significant amount of time. [24,25]

Sputtering has various advantages when compared to the other popular PVD technique - evaporation. Sputtering provides better film thickness control, has large area targets (improves film thickness uniformity), provides better film composition and properties control based on process conditions, provides the ability to sputter-clean the substrate prior to film deposition (allows for removal of thin native oxide layers), and reduced device damage from X-rays. [26]

In this project, all the metals – nickel, aluminum, and α-phase tantalum – are deposited using sputtering. The exact purpose of each metal is described in Chapter 3. Nickel and aluminum were sputtered on the PE 4400 tool, whereas α-tantalum was sputtered on the CVC 601 tool. The PE 4400 boasts a load-lock system that allows quick pumpdown of the deposition chamber. The CVC 601, on the other hand, boasts temperature control of the substrate, which is useful for the α-tantalum film deposition. However, the CVC 601 does not have a load-lock system and therefore takes several hours to pump down to the

required pressure. The exact sputter recipes for all three films can be found in the Appendix.

2.4.4 Plasma Enhanced Chemical Vapor Deposition

Chemical vapor deposition (CVD) involves formation of a solid film on a substrate by the reaction of vapor-phase chemicals (reactants) that contain the required constituents. CVD processes do not react with or consume the substrate (unlike thermal oxidation of silicon, for example). The basic procedure for a CVD process is as follows:

1. Reactant gases diffuse into stagnant layer from main gas flow region.
2. Reactant gas species adsorbed on substrate.
3. Adatom migration and film-forming chemical reaction, enhanced by a plasma.
4. By-products desorbed from substrate.
5. By-products diffuse into main gas flow region.

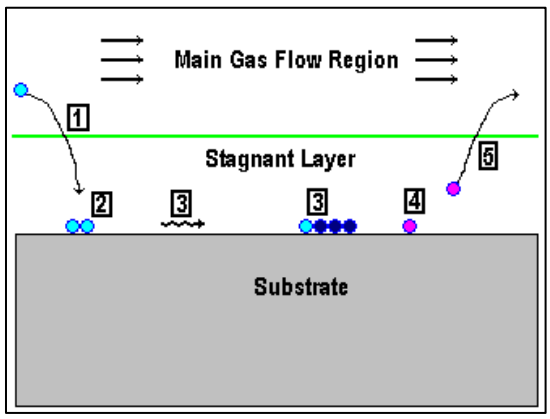

Figure 2.10: Typical CVD Process [26]

The difference with a plasma-enhanced CVD system is that a RF-induced glow discharge (commonly called plasma) transfers energy to the reactant gases. This leads to higher deposition rates, higher sticking coefficients for reactants, stronger bonds to surface, improved step coverage, good gap filling, and lowers the required temperature for the deposition process at the expense of film purity and stoichiometric uniformity. [26]

In this project, PECVD is used for depositing an inter-layer SiO_2 dielectric using a TEOS precursor on the P-5000 tool. The chemical reaction from TEOS to silicon dioxide is shown in Eq. 2.12.

$$Si(OC_2H_5)_4 + O_2 \rightarrow SiO_2 + \text{by-products} \qquad \textbf{Eq. 2.12}$$

The film purity and stoichiometric uniformity are not critical to the device performance, but physical considerations such as step coverage and thickness control are important. Therefore, PECVD is a perfect deposition technique to use to deposit the inter-layer SiO_2 dielectric. The exact recipe details can be found in the Appendix.

2.4.5 Thermal Oxide Growth

One of the major reasons silicon is so popular for use as a substrate for microelectronic applications is because it oxides readily in high temperatures to form SiO_2, which has excellent surface, dielectric, and insulating properties. It also has a high melting point of ~1700 °C, and a thermal coefficient similar to that of silicon.

There are two simple ways silicon dioxide can be grown on a silicon surface – dry or wet oxidation. Dry oxidation happens in a pure oxygen environment, whereas wet oxidation happens in presence of water vapor. Wet oxidation is about 600x faster than dry oxidation due to higher concentration of dissolved oxidant in the gas. Eq. 2.13 and 2.14 show the two chemical reactions involved, which happen above 900 °C.

$$Si + O_2 \rightarrow SiO_2 \qquad \textbf{Eq. 2.13}$$

$$Si + 2H_2O \rightarrow SiO_2 + 2H_2 \qquad \textbf{Eq. 2.14}$$

Oxide growth consumes silicon as part of the reaction at a ratio of about 1:0.44. This means that a 100 Å oxide growth will consume 44 Å of silicon. The exact oxide growth modeling is well-understood using the Deal and Grove model. [25]

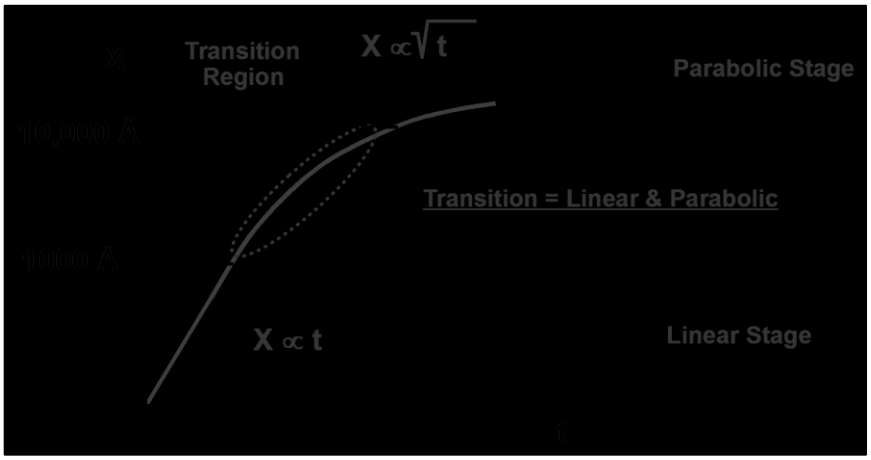

Figure 2.11: Deal and Grove Model for Silicon Oxidation [27]

The Deal and Grove model shows two major stages of oxide growth – a linear stage where thickness growth is linearly proportional to oxidation time, and a parabolic stage

where the thickness is parabolically proportional to oxidation time. Eq. 2.15 and 2.16 show the thickness X as it depends on time t and the parameter τ, which is related to initial conditions, for the linear and parabolic stages respectively.

$$X_{linear} = \frac{B}{A}(t + \tau) \qquad \textbf{Eq. 2.15}$$

$$X_{parabolic} = \sqrt{B(t + \tau)} \qquad \textbf{Eq. 2.16}$$

Here, the quantity *(B/A)* is called the linear rate constant and it depends on the surface reactant rate, oxidant concentration in the oxide, and the number of oxidant molecules incorporated per unit volume. The quantity B is called the parabolic rate constant and it depends on diffusivity, oxidant concentration in the oxide, and the number of oxidant molecules incorporated per unit volume.

In this project, thermal oxidation is used to grow a 5000 Å wet pad oxide to insulate the devices from the substrate and from each other. The exact recipe for this pad oxide can be found in the Appendix.

2.4.5.1 Nickel Thermal Oxidation

The concepts of thermal silicon oxidation are extremely important to understand thermal nickel oxidation as well. Similar to silicon thermal oxidation, nickel thermal oxidation also results in a thickness increase. This theoretical increase can be calculated as shown in Eq. 2.17 – 2.21.

$$\text{Mass of 1 cm}^2 \text{ Ni film of thickness } t_{Ni} = t_{Ni} * d_{Ni} \qquad \textbf{Eq. 2.17}$$

$$\text{Number of Ni atoms} = \frac{t_{Ni} * d_{Ni}}{Atomic\ Weight\ of\ Ni} * Avogadro's\ Number \qquad \textbf{Eq. 2.18}$$

$$Number \text{ of NiO molecules} = \frac{\text{t}_{\text{NiO}} * d_{NiO}}{Atomic\ Weight\ of\ NiO} * Avogadro's\ Number \qquad \textbf{Eq. 2.19}$$

$$\text{Now, Number of Ni atoms} = \text{Number of NiO molecules} \qquad \textbf{Eq. 2.20}$$

$$\therefore \frac{t_{NiO}}{t_{Ni}} = \frac{d_{Ni} * Atomic\ Weight\ of\ NiO}{d_{NiO} * Atomic\ Weight\ of\ Ni} = \frac{8.902 * 74.69}{6.67 * 58.69} = 1.7 \qquad \textbf{Eq. 2.21}$$

Therefore, a completely oxidized nickel oxide film should be about 1.7x thicker than the initial nickel film, assuming bulk densities.

2.5 Analysis Techniques

A variety of analysis techniques will be employed in order to characterize the devices fabricated, in addition to blanket nickel oxide films. These techniques will provide electrical, compositional, optical, structural, and film morphology information about the devices and the nickel oxide film.

2.5.1 Electrical Analysis

2.5.1.1 Current-Voltage Analysis

Current-voltage analysis (I-V) is used to examine the current conduction through the MIM devices as the voltage is sweeped. This kind of examination reveals various kinds of information about the devices. The shape of the curve obtained speaks to the device's ohmic behavior (or lack thereof). The slope of a linear I-V curve gives the device's electrical resistance, following Ohm's law. It can also yield a device's breakdown strength if the device breaks down at a certain voltage. It can also indicate any resistance switching characteristics if the device switches resistance states at a particular voltage bias. A varying current conduction profile depending on the direction of sweep (positive to negative vs. negative to positive) can indicate hysteresis. Performing this I-V testing on differently sized devices can show area effects, and lend credence to suspicions of conduction filament formation if the current flow is not as predicted by area scaling.

2.5.1.2 Current-Time Analysis

Current-time analysis (I-t) is used to examine the conduction behavior over time of the NiO MIM devices. Varying current conduction over time can potentially show clues of conduction mechanism of the film. A flat constant current profile is indicative of an ideal ohmic resistor. An increasing current profile can indicate increasing charge buildup or formation of permanent conduction paths. A decaying current profile indicates the destruction of conduction paths and potentially oxidation of the electrodes due to high current flow. An oscillating current profile from a low resistive state to a high resistive state can show evidence of resistive switching, for which, the root cause must be modeled. Similar I-t analysis was conducted at IBM and Motorola to model the conduction mechanism of high-k HfO_2 films and BST films respectively. [28] [29]

2.5.1.3 Resistance-Temperature Analysis

Since microbolometers are electrically sensitive to infrared radiation, they should show change in resistance measured upon exposure to a thermal source. This is exactly the test used in this project to demonstrate the viability of nickel oxide as an infrared-sensitive film. A small lamp with controllable intensity is put 1 cm away from the microbolometer while a multimeter is used to measure the change in resistance for each shift in intensity. A diode circuit (Figure 2.12) is used to translate the arbitrary intensity values to temperature shifts by measuring its on-voltage and using the fact that the on-voltage should shift -2.2 mV/°C. This information is then used to calculate the TCR of the microbolometers. [25]

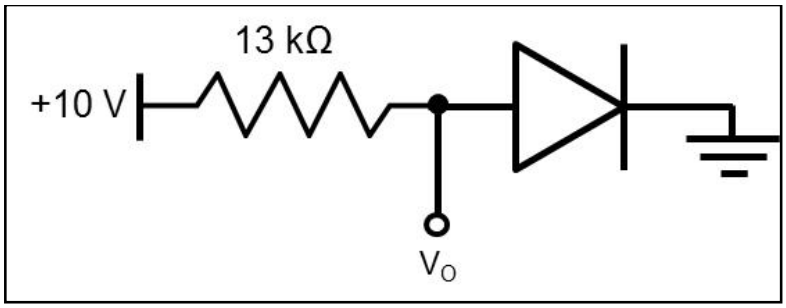

Figure 2.12: Diode circuit used to measure temperature change for lamp from off to full intensity

2.5.2 Structural Analysis

2.5.2.1 Transmission Electron Microscopy

Transmission electron microscopy (TEM) is an imaging technique that extends beyond the resolution of typical optical spectroscopy. Electrons are passed through the film in investigation. The resulting diffraction pattern is observed on a fluorescent screen, on photographic film, or detected by a CCD camera.

TEM is able to resolve images down in the sub-nanometer regime, which puts its resolution in the range of the radii of many elements. This level of imaging uses electrons for imaging, rather than standard visible light used in traditional microscopes, or even X-rays that are used in X-ray diffraction studies, because electrons have a very small de Broglie wavelength, λ, as defined by Eq. 2.22:

$$\lambda = \frac{h}{p} \qquad \textbf{Eq. 2.22}$$

where h is Planck's constant, and p is the momentum of the electron.

The contrast for TEM images is due to difference in absorption of electrons (bright field) in the sample, due to variation in composition and thickness of the material, for small magnifications. Another mode for contrasts is based on the atomic number of the elements imaged, and is thus called Z-contrast. At higher magnifications, the intensity of the image is affected by complex wave interactions. TEMs can also be altered to observe modulations in chemical composition, crystal orientation, and even regular absorption based imaging.

The downside to TEM is that they require very careful and tedious, and therefore expensive, sample preparation. To observe quantum effects of electrons, the sample thickness must be between 0.5 and 2.0 μm. Focused ion beam (FIB) is the typical method for TEM sample preparation.

Due to TEM's extremely high magnifications and excellent contrast differentiation between different materials, it is a perfect analysis for observing and confirming oxidation of nickel. It is possible to easily distinguish areas of high oxygen concentration from areas of lower oxygen concentration. It can also be used to observe grain size and crystal structure (if any) of the different thin films. It can also detect the presence of any thin interfacial layers between films that have grown between process steps. Combined with energy dispersive X-ray spectroscopy (EDS), TEM can be an even more powerful materials analysis technique.

2.5.2.2 Energy Dispersive X-ray Spectroscopy

Energy dispersive spectroscopy (EDS) is a powerful analytical technique used for the elemental analysis of a sample. The analysis investigates the interaction of X-rays and the sample.

EDS relies on the fundamental principle that each element has a unique atomic structure, which allows a unique set of peaks on its X-ray spectrum. [30] The sample is exposed to a high-energy beam of charged particles (usually electrons) to stimulate the emission of characteristic X-rays from the sample. Normally, an atom contains unexcited (ground state) electrons in discrete energy levels, bound to the nucleus containing the neutrons and protons. An electron from an inner shell close to the nucleus may be excited by the incident beam, thereby ejecting it from its shell and leaving behind an electron vacancy (or hole). An electron from an outer, higher-energy, shell then fills this vacancy and the difference in energy is emitted as X-ray photons (see Figure 2.13).

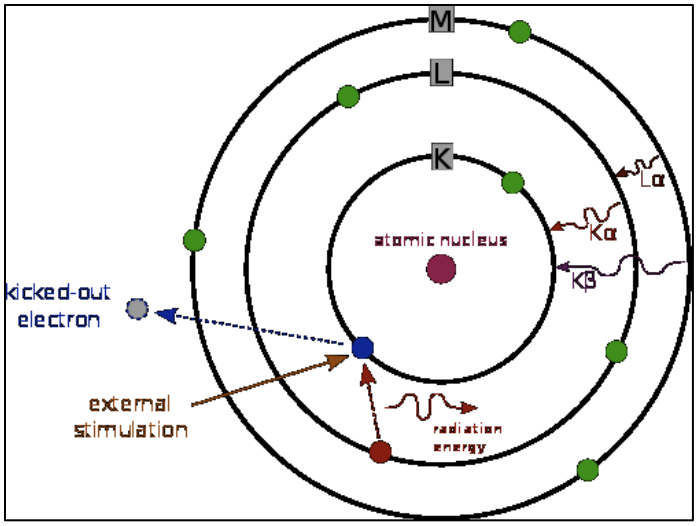

Figure 2.13: Principles of EDS

The X-ray emission from a sample is measured by an X-ray detector, after going through the necessary focusing optics. Figure 2.14 shows a schematic layout of an EDS system. Since the energy of the X-rays are related to the difference in energy between the two shells, and of the atomic structure of the element from which they were emitted, this allows the composition of the sample to be measured. [30]

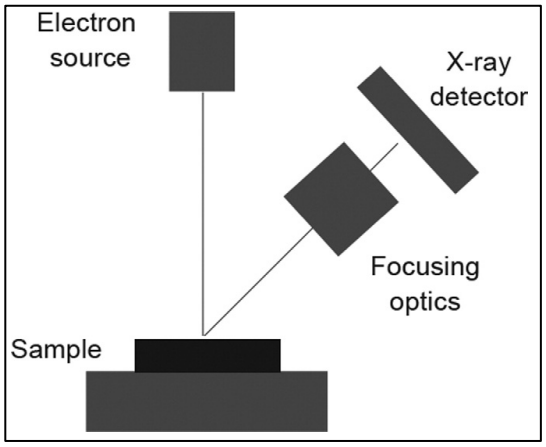

Figure 2.14: Schematic principle of EDS [31]

2.5.2.3 X-ray Diffraction

In 1919, A.W. Hull wrote, in a paper titled "A New Method of Chemical Analysis", that "… every crystalline substance gives a pattern; the same substance always gives the same pattern; and in a mixture of substances each produces its pattern independently of the others." [32] The X-ray diffraction (XRD) pattern of a pure material is its equivalent of a fingerprint. This technique is thus ideally suited for characterization and investigation of unknown films, based on documented data.

An electron, when in an alternating electromagnetic field, oscillates with the same frequency as the field. Therefore, when an X-ray beam is shot at an atom, the electrons of that atom start oscillating with the same frequency as the incoming beam. For almost all directions, all the combining waves will be out of phase and thus will destructively interfere, and no resultant energy leaves the sample. However, for a crystalline sample, in very few directions, constructive interference will be observed. The waves will be in phase and well-defined X-ray beams will leave the sample at very specific directions. These X-ray beams are picked up by the X-ray detector at those specific angles, and a characteristic XRD spectrum for a particular sample is created. The observed peaks can then be compared with simulated and tabulated data to characterize the sample.

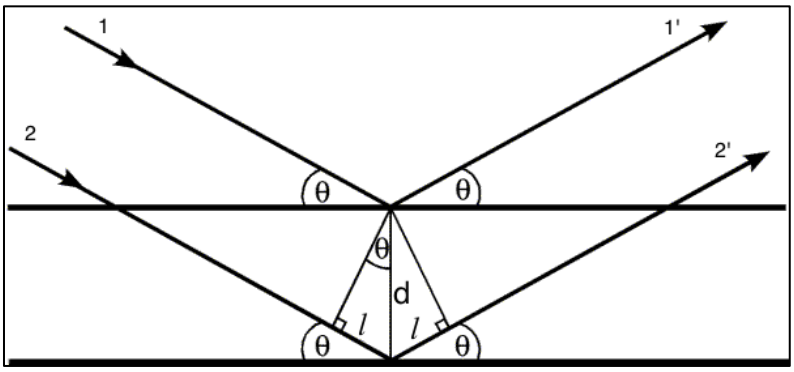

Figure 2.15: Bragg's Law

The principle behind XRD is based on Bragg's law. Consider an X-ray beam incident on a pair of parallel planes, separated by an interplanar spacing *d* (refer to Figure 2.15). Two parallel incident rays 1 and 2 make an angle θ with these planes. A reflected beam of maximum intensity will result when the waves represented by 1' and 2' are in phase. The difference in path length between 1 to 1' and 2 to 2' must then be an integer number of wavelengths, λ. We can express this relationship mathematically in Bragg's law, as shown in Eq. 2.23 (where *n* is an integer greater than zero).

$$2d\sin(\theta) = n\lambda \qquad \textbf{Eq. 2.23}$$

The process of reflection is described here in terms of incident and reflected (or diffracted) rays, each making an angle θ with a fixed crystal plane. Reflections occur from planes set at an angle θ with respect to the incident beam and generate a reflected beam at an angle 2θ from the incident beam's path.

Therefore, the unit cell dimensions determine the possible 2θ values where reflections with constructive interference are possible. However, the distribution of the density of electrons in the unit cell defines the intensities of these reflections. The highest electron density is found around atoms. Planes going through areas with high electron density will reflect strongly, whereas planes with low electron density will give weak intensities.

A typical XRD result will show the measured reflected x-ray intensities versus the detector 2θ values. Each reflection is fully defined when the *d*-spacing, the intensity (area under the peak), and the miller indices *h*, *k*, *l* of the lattice are known. [32] The *d*-spacing can be calculated as shown in Eq. 2.24. Together, Eq. 2.23 and 2.24 can be used to identify the miller indices *h*, *k*, *l* of the crystal lattice, if the lattice parameter *a* is known.

$$d = \frac{a}{\sqrt{h^2 + k^2 + l^2}} \qquad \textbf{Eq. 2.24}$$

2.5.3 Optical Analysis

Ellipsometry is an optical technique used for the investigation of dielectric and physical properties of a film as they are related to optical measurements. Specifically, single angle single wavelength ellipsometry can yield the thickness of a film as well as the real and imaginary refractive indices. Eq. 2.25 shows the real and imaginary components of a sample's complex refractive index n_S^*:

$$n_S^* = N_S - iK_S \qquad \textbf{Eq. 2.25}$$

where N_S is the real component, K_S is the imaginary component, and i is the imaginary unit such that i^2 = -1. The real part describes refraction, the imaginary part accounts for absorption. Both N_s and K_s vary based on wavelength of light. A perfectly transparent film has no imaginary component, for a given wavelength.

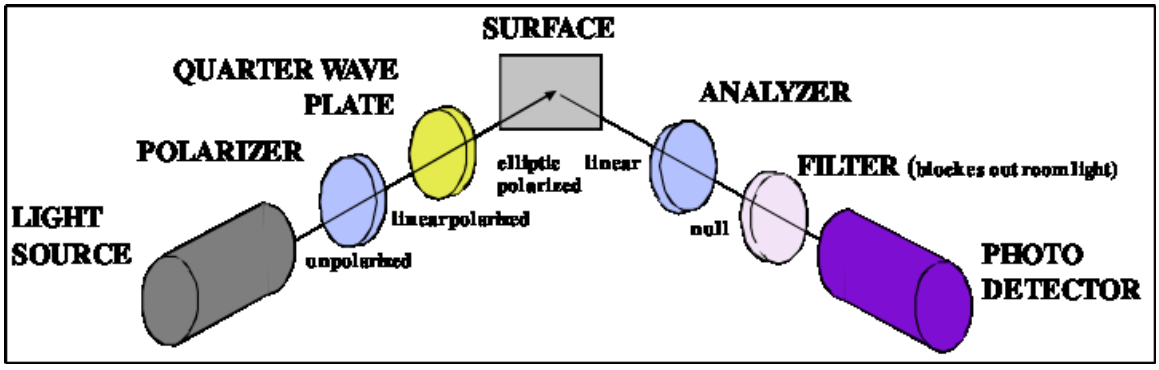

Figure 2.16: Ellipsometer Setup [22]

Figure 2.17: Passage of light through a null ellipsometer [33]

The light source used is a source of unpolarized single wavelength light, which, upon traversing the polarizer with its transmission axis at an angle *P* relative to the plane of incidence (the horizontal in Figure 2.17), becomes linearly polarized. It next encounters a quarter-wave-plate (QWP) with its fast axis fixed at an angle -45° to the plane of incidence. This linearly polarized light incident to the QWP can be resolved into components parallel to the QWP axes (indicated by the dotted lines). The QWP introduces a 90° phase shift between these components, and the polarization of the emergent light is elliptical with semi-major axis *a* and semi-minor axis *b*. As the angle *P* is varied, *a* and *b* change, but the orientation of the ellipse remains fixed at 45° to the plane of incidence. The *s* and *p* components of the light incident to the surface, e_s and e_p, are always equal in magnitude. After reflecting off the surface, the light passes through a

second polarizer (called the analyzer) with its transmission axis oriented at an angle A relative to the plane of incidence. These angles A and P are adjusted alternately until the analyzer's axis of polarization is perpendicular to the azimuth of the incoming linearly polarized light, creating a null. Thus, no light is transmitted to the detector.

A measurement with the ellipsometer therefore involves measurement of the angles A and P that produce a null at the detector. These angles are used to calculate the light parameters Δ (relative phase retardation) and Ψ (where $\tan(\Psi)$ is the relative amplitude diminution). These light parameters can then be used alongside Fresnel equations to calculate the complex index of refraction and/or thickness of the film in study. Thickness values that correspond to these parameters repeat with integer multiples of the light source's wavelength, so the approximate thickness must be known. [22] [33]

Chapter 3

Design and Fabrication

Investigation of any material's specific properties requires proper planning, design of experiment, and its execution. To investigate the bolometric properties and its feasibility for use as a bolometric sensor, serpentine microbolometric resistors were designed with nickel oxide as the infrared-sensitive material. To investigate the resistive properties of nickel oxide and its feasibility for use as a resistive memory element, metal-insulator-metal (MIM) diodes were designed to study the various current conduction effects observed due to different stimuli. Both the structures were designed to be on the same die, the layout for which was designed using the Mentor Graphics suite. Lithography masks were also made in-house at the RIT e-beam laboratory, and the devices were fabricated at the RIT Semiconductor and Microsystems Fabrication Laboratory (SMFL) together using the same process flow. Their electrical performance of the fabricated devices was also tested at the RIT SMFL's electrical testing laboratory.

3.1 Layout and Design

3.1.1 Circuit Design

3.1.1.1 Microbolometer

The microbolometers were tested as an array of pixels, thus forming an imager. Each pixel was designed as a voltage divider circuit as shown in Figure 3.1.

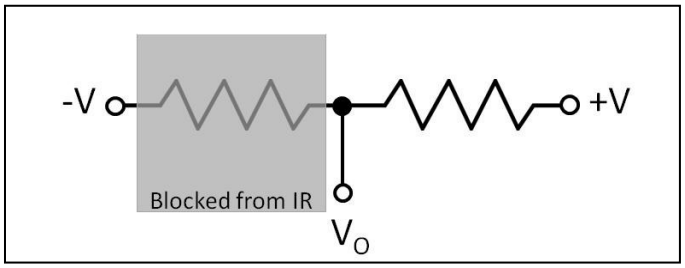

Figure 3.1: Microbolometer Pixel Circuit

Both resistors are designed to be identical, but likely are a bit different from each other due to slight topography differences. Each resistor is designed as a serpentine resistor to maximize the resistance of each resistor (see Figure 3.2). This is done because the TCR of the device defines the percent change in resistance per degree; therefore, a larger initial resistance leads to a larger (in terms of actual ohms) change in resistance as well, and is thus easier to measure.

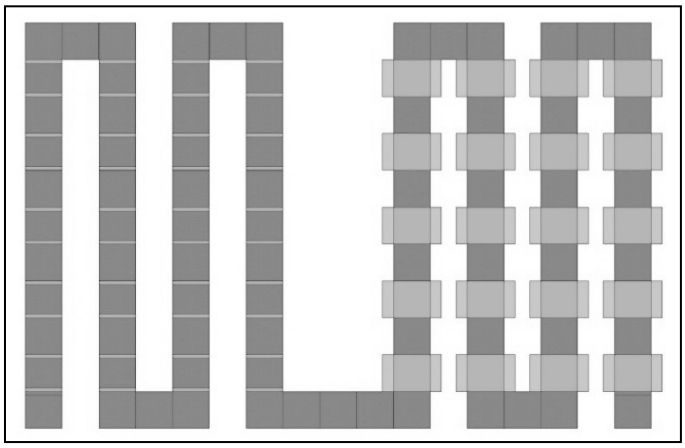

Figure 3.2: Microbolometer Pixel Layout

One resistor of the circuit is blocked from incoming infrared radiation by a thick PECVD SiO_2 layer, and the other is exposed to it. The sensitive resistor is built as an air-bridge between two α-Ta (described in section 3.2.1.4) electrodes to thermally isolate it from the substrate so it does not easily dissipate the heat gained from the incoming infrared radiation. A sacrificial layer of photoresist was used to support the nickel during its deposition, and was stripped after nickel patterning. Figure 3.3 depicts the cross-section of the microbolometer pixel, minus the serpentine shape.

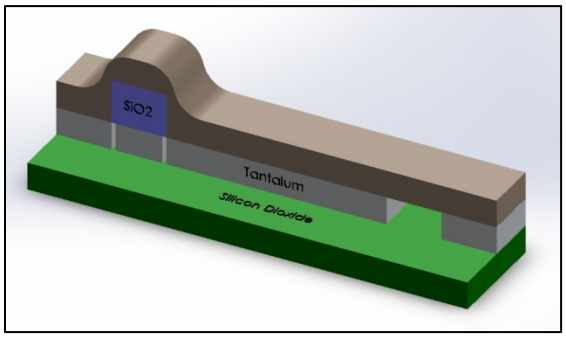

Figure 3.3: Cross-section of a microbolometer pixel

Using a voltage divider circuit compensates for the ambient heat of the system as both resistors change identically for the heat in the system. When no infrared radiation is incoming, the +V and –V power supply should be adjusted such that the voltage readout at V_0 is close to 0 V. Then, the device is exposed to infrared radiation and any change in V_0 happens due to a change in resistance of the sensitive resistor. If this voltage change is measured to be significant, then the NiO microbolometer works as a MEMS device.

3.1.1.2 MIM Device

Six sizes of MIM devices (ranging from 0.5 μm^2 to 10 μm^2) were fabricated in each replication of the MIM device array. The diodes are designed as square vertical capacitors, with α-Ta as the bottom electrode, NiO as the insulator, and Al as the top electrode. PECVD SiO_2 is used as a barrier layer to prevent shorting between the electrodes. See Figure 3.4 for the cross-section layout.

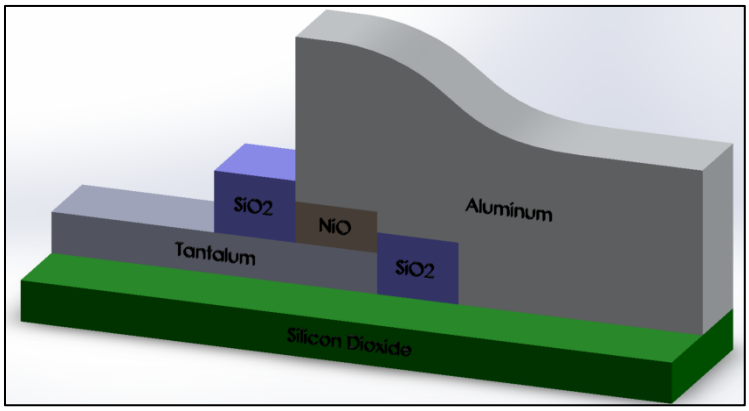

Figure 3.4: Cross-section of a MIM device

3.1.2 Mask Layout

The designs for the devices for this project were made using the Mentor Graphics suite. [22] Both microbolometers and MIM devices were included on a 5 mm x 5 mm die. The die contains one 16-pixel array of microbolometers, 6 replicates of the 8-pixel array of microbolometers, and 6 replicates of the MIM devices array containing multiple sizes in each. See Figure 3.5, 3.6, and 3.7 for the layout design of the 16-pixel microbolometer array, 8-pixel microbolometer array, and the MIM device array respectively. Figure 3.8 shows the complete die layout.

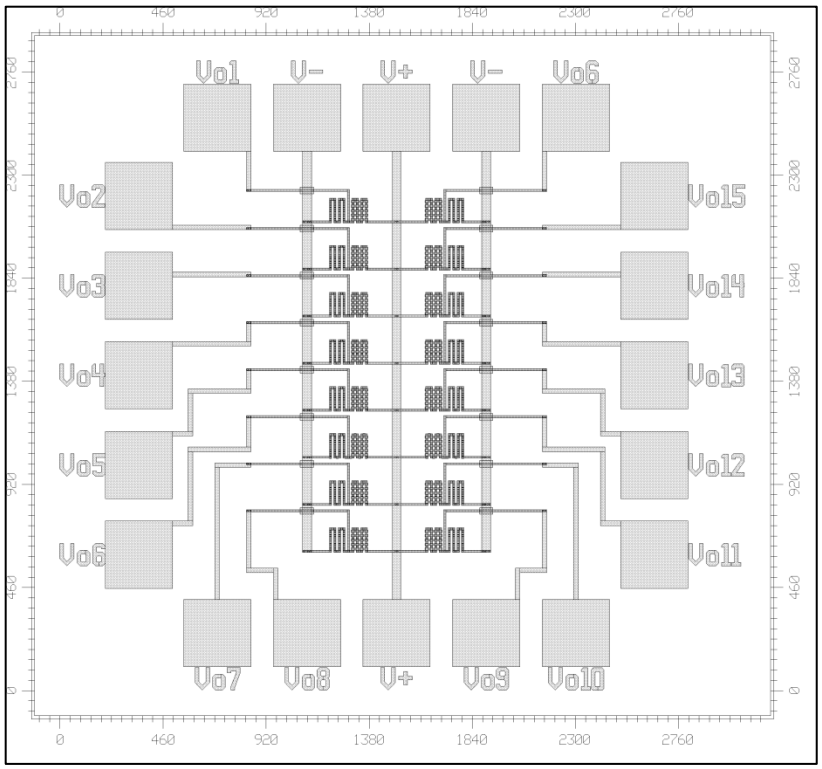

Figure 3.5: 16-Pixel Microbolometer Array Layout

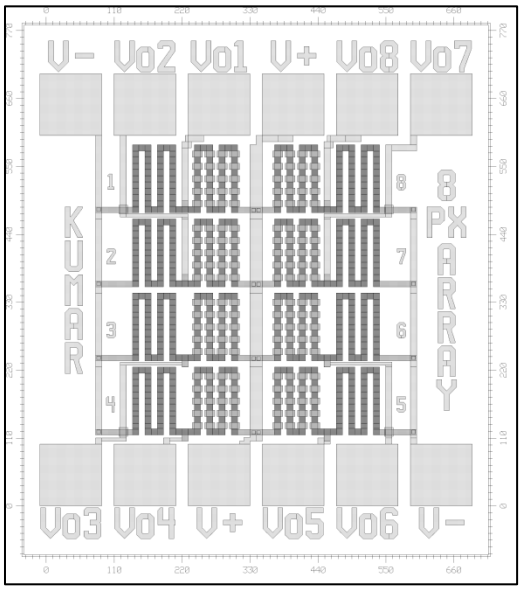

Figure 3.6: 8-Pixel Microbolometer Array Layout

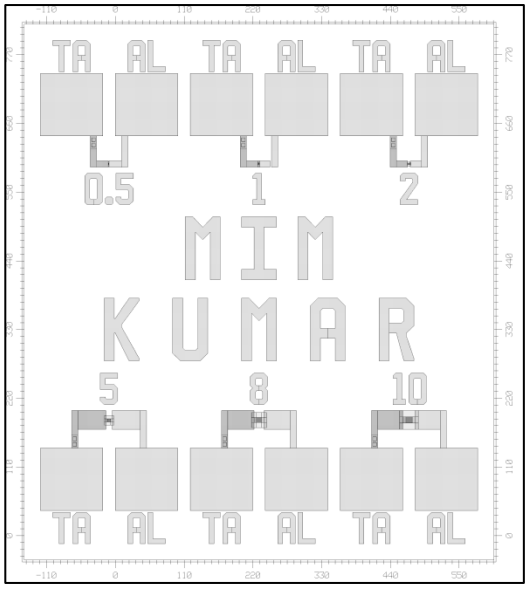

Figure 3.7: MIM Device Array Layout

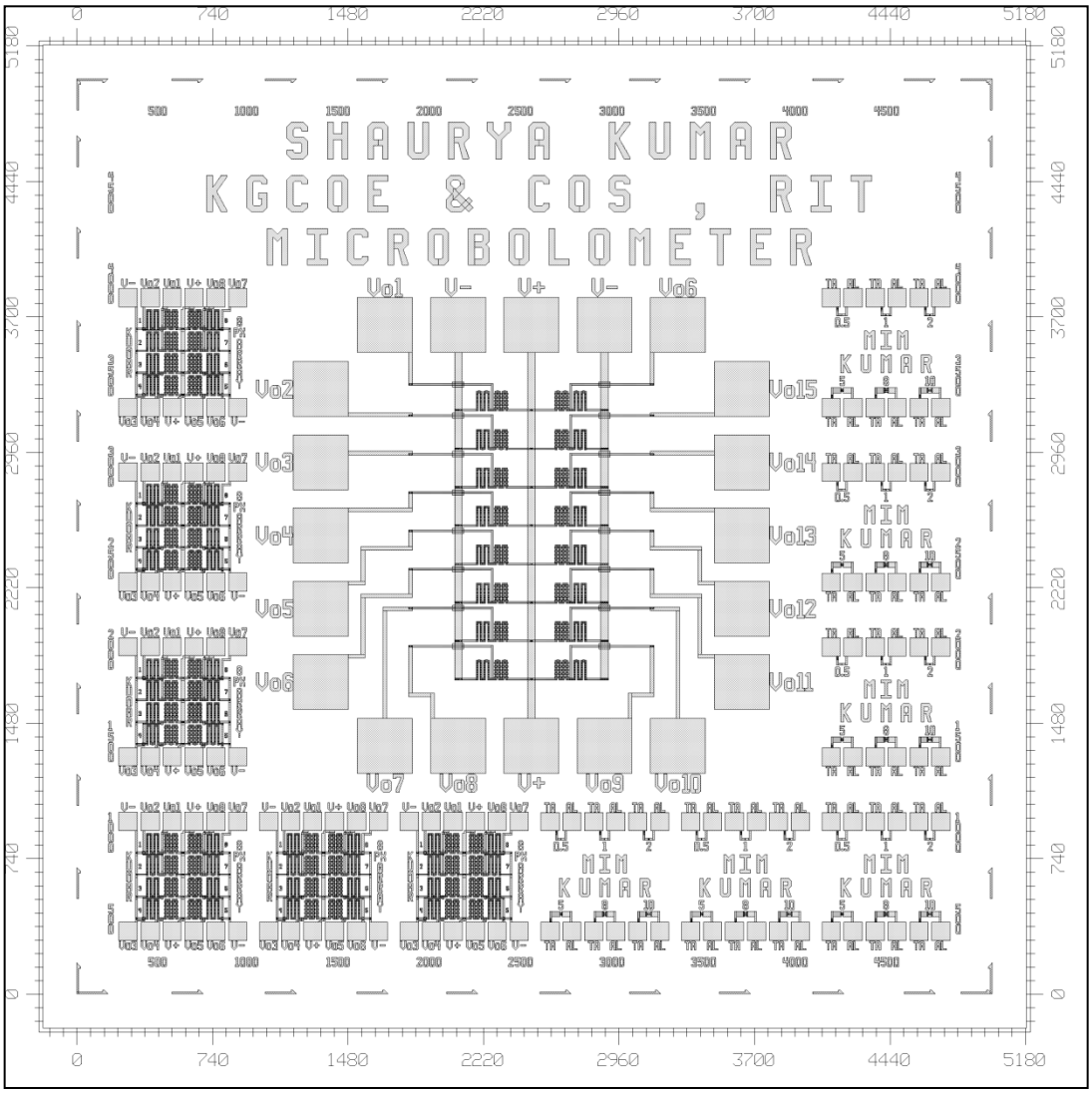

Figure 3.8: Complete Die Layout

The layout requires 6 mask layers – α-Ta, PECVD SiO_2, sacrificial photoresist, α-Ta contact cut, Ni, and Al. These mask layers, along with inverse masks for Ni and Al, were printed on 2 mask plates using the MEBES e-beam tool, for use in the ASML i-line stepper. The minimum feature size was 0.5 μm.

3.2 Fabrication Process Flow

A detailed process flow was created taking into account the required process steps for both the microbolometers and the MIM devices. The entire process included 28 process steps, including seven (7) lithographic levels. A brief visual depiction of the process flow is shown in Figure 3.9.

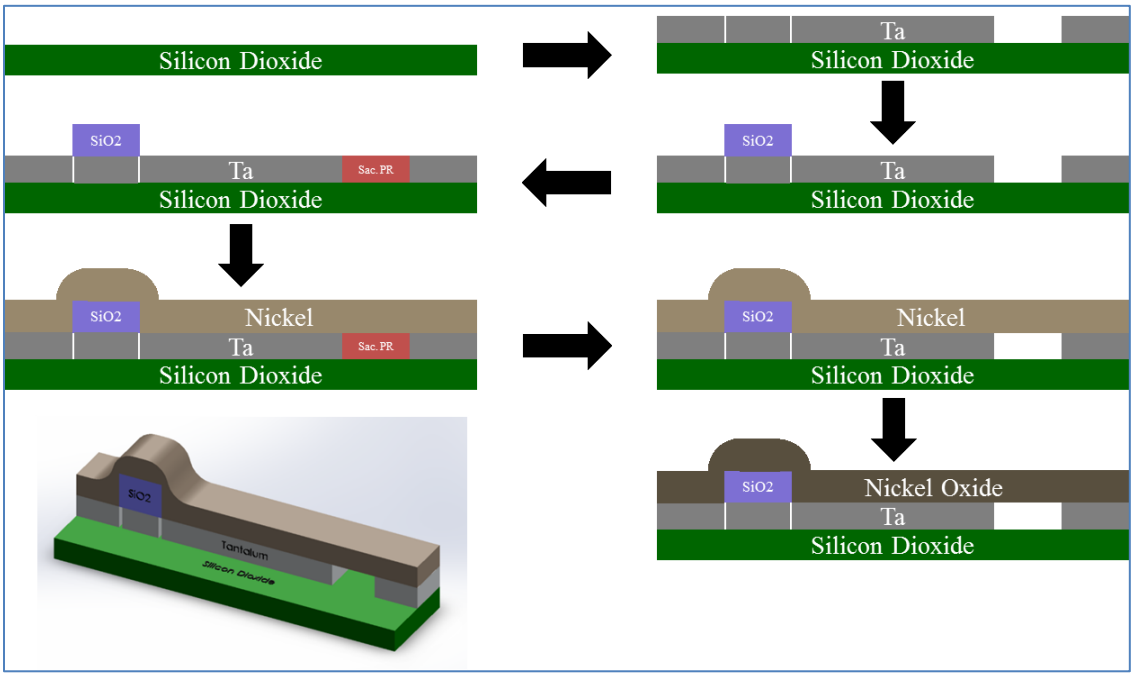

Figure 3.9: Process Flow Overview

All lithography processes was done on the SSI track (used for photoresist coating and developing) and the ASML stepper (used for photoresist exposure). Recipe details for each step can be found in the Appendix.

Five (5) bare Si wafers, 5 process and 5 test wafers, were obtained. The test wafers were used to characterize any critical step parameters (such as a film deposition time, or etch rate) prior to applying it to the process wafers.

3.2.1.1 RCA clean and HF dip

The process started off with a standard RCA clean step on the MOS RCA bench for all wafers to remove any contaminants, organic and inorganic, from the bare silicon wafer surface. It was followed up with a 10 second dip in 50:1 diluted HF solution with surfactant to remove any thin layers of native oxide.

3.2.1.2 Level zero lithography and etch

Next is level zero lithography using the standard "combi reticle" made available to all users. This defines the pattern of the wafer alignment marks. The subsequent silicon etch in the chamber 2 of the DryTek Quad plasma etch tool using recipe ZEROETCH etches into the silicon to create the necessary wafer alignment marks required for subsequent lithographic steps. The wafers are then stripped off the remaining photoresist using the standard strip recipe in the wet solvent strip. This is followed by a standard SRD (spin, rinse, dry) step.

3.2.1.3 Pad oxide growth

Next comes the growth of a thick pad oxide to insulate the devices from the remainder of the substrate, and from each other. The first step in this is a standard RCA clean step to ensure that the furnace tubes are not exposed to excessive wafer contaminants and

particles, and a clean and stoichiometrically pure oxide is grown. Recipe 350 in Tube 1 of the Bruce Furnace is used for the wet thermal oxidation of the silicon. This grows a 5000 Å thick oxide, which is confirmed by subsequent spectrometric measurements using the Prometrix SpectraMap.

3.2.1.4 α-phase Tantalum – Sputter and Patterning

Next comes the deposition of a bottom electrode metal for the bolometer and the MIM device. In the choice for this metal, the choice for the top electrode metal and other process constraints had to be considered. Nickel etches in the same wet chemistry as aluminum, and therefore aluminum could not be chosen as a bottom electrode. Tantalum, specifically α-phase tantalum, was chosen due to its well-characterized deposition and etch processes, and its resistance to aluminum wet etchant. Tantalum etches controllably in a SF_6 plasma or in NaOH/KOH wet chemistry. [34] α-phase tantalum is chosen over β-phase tantalum because α-Ta has a much lower resistivity than β-Ta, and is this more suitable for use as an electrode metal. [35]

However, the process requirements of sputtering α-Ta are very rigid without too much margin for error, and therefore this material requires careful processing. The top surface of α-Ta is known to readily oxidize in air if left out for several days, and hence it requires quick throughput to the next step. Resistivity measurements confirmed formation of the α-phase of tantalum.

After fabrication, it was realized that the Pilling-Bedworth ratio of tantalum's oxide, Ta_2O_5, is 2.44 – indicative of large compressive stress on the film leading to cracking and fracture of the oxide. Nevertheless, it is still extremely resistant to localized attack by pitting corrosion. [36]

2500 Å of α-Ta is sputtered on the CVC 601 tool and the thickness is confirmed using a profilometric measurement on a test wafer, using Kapton tape as a mask. After sputtering α-Ta, the wafers undergo Level 1 metal lithography (which involves a thicker coating of photoresist). The test wafer is used to observe α-Ta's etch rate of using the α-Ta etch recipe in the LAM 490 plasma etcher. Using this measured etch rate, α-Ta is then plasma-etched off the device wafers. The wafers are then stripped off the remaining photoresist using the standard strip recipe in the wet solvent strip. This is followed by a standard SRD (spin, rinse, dry) step.

3.2.1.5 PECVD SiO_2 – Deposition and Patterning

Recipe A6-4KA is used on the P-5000 tool to deposit 4000 Å of PECVD SiO_2, using TEOS as a precursor. The wafers then undergo Level 2 standard lithography to create a photoresist pattern on the SiO_2. A test wafer with blanket 4000 Å of PECVD SiO_2 is used to measure its etch rate in 10:1 Buffered HF with surfactant. This measured etch rate is then used to calculate the appropriate etch time while etching the PECVD SiO_2 off the device wafers. The wafers are then stripped off the remaining photoresist using the standard strip recipe in the wet solvent strip. This is followed by a standard SRD (spin, rinse, dry) step.

3.2.1.6 α-phase Tantalum Contact Cut Etch

The device wafers undergo Level 5 metal lithography for contact cut etch. The α-Ta is then partially etched to create contact cuts in the electrodes which would be later filled in with aluminum. The wafers are then stripped off the remaining photoresist using the standard strip recipe in the wet solvent strip. This is followed by a standard SRD (spin, rinse, dry) step.

3.2.1.7 Sacrificial Bridge Photoresist

The device wafers undergo Level 3 standard lithography to create a photoresist pattern on the wafers. The remaining photoresist will serve as a buffer support film for the upcoming nickel deposition, and will subsequently be stripped to create a nickel air-bridge.

3.2.1.8 Nickel – Deposition and Patterning

The 2100 Å of nickel is sputtered on the wafers using the PE 4400 sputter tool. The thickness is confirmed using a profilometric measurement on a test wafer, using Kapton tape as a mask. The Kapton tape is observed to leave a lot of residue upon removal, but nevertheless, profilometric measurement could be conducted in several areas. The wafers then undergo Level 4 metal lithography to create the photoresist pattern. The test wafer is then used to measure the etch rate of nickel in the aluminum wet etchant. Using this measured etch rate, Ni is then wet-etched off the device wafers. The wafers are then stripped off the remaining photoresist using the standard strip recipe in the wet solvent

strip. This solvent strip step is also expected to strip the sacrificial photoresist from the previous step, leaving behind a nickel air-bridge.

However, it is observed that the photoresist does not strip, even after repeated runs of the solvent strip recipe. At the same time, nickel is observed to start peeling-off from non-die areas, possibly due to thermal heating from the solvent strip step causing excessive stress between the nickel and its underlying SiO_2. The nickel in the device areas is observed to continue to adhere to the underlying tantalum. Since the removal of the sacrificial bridge photoresist is critical to the functioning of the devices, the wafers are put through an oxygen plasma hard-ash (recipe FF) step in the GaSonics asher. This plasma ash step not only confirms the removal of the sacrificial bridge photoresist, but it also strips off a significant amount of peeling nickel from the non-die areas of the wafers, leaving behind usable device wafers. Figure 3.10 shows a picture of the wafer after the hard-ash. This is followed by a standard SRD (spin, rinse, dry) step.

Due the wafers' exposure to the oxygen plasma, the α-Ta is observed to have blackened and appears rougher on the surface under a microscope. Figure 3.11 shows a microscope image of an MIM device after fabrication showing the tantalum oxidation on the left. It is likely that the surface, and maybe even underlying layers of the α-Ta have been oxidized from the oxygen plasma. This is not ideal as α-Ta is being used as an electrode metal and it is preferable to keep it metallic, rather than oxidizing it. It is also likely that the Ni top-surface has been oxidized, but that is not a huge problem, as the rest of the Ni will be thermally oxidized anyway.

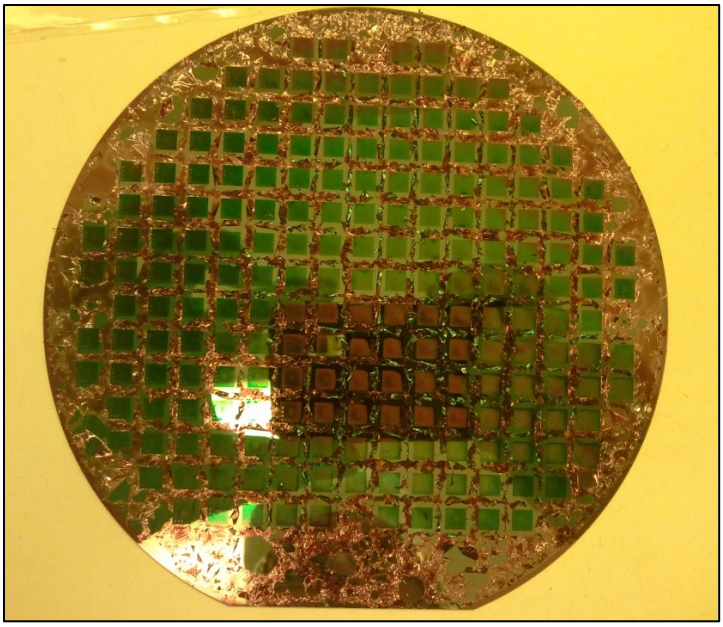

Figure 3.10: Post-ash nickel peeling from non-die areas

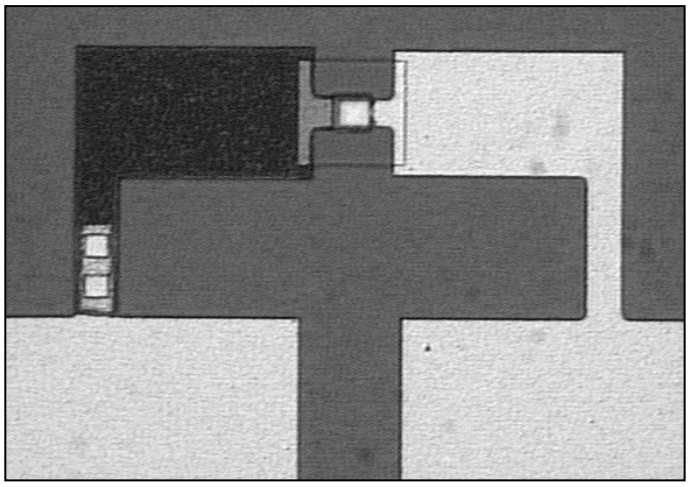

Figure 3.11: Post-fabrication microscope image of MIM shows oxidized tantalum on left

3.2.1.9 Nickel thermal oxidation

Nickel, along with most other metals, is viewed as a contaminant in the furnace tubes, and therefore, SMFL rules do not allow for oxidation of nickel in the furnaces. However, one of the tubes, Tube 8, is already contaminated with other metals and is restricted for such use. It is a 4" tube however, and therefore, the 6" wafers must be placed horizontally, device side up, to fit in the tube.

A blanket Ni coated test wafer is used to verify the oxidation process. It is put in the furnace at 500 °C for 5 hours. The film on the wafer post-furnace run appears to be greenish-yellow in color and has a very high resistivity (beyond the measurement range for the ResMap tool). There seem to be no adhesion problems. Profilometric measurements indicate that the thickness has also increased from ~2100 Å to ~3500 Å, a ~1.67x increase. All three of these observations (color, resistivity, and thickness increase) are consistent with expectations based on theory and the recipe is suspected to oxidize the nickel film completely. The device wafers are then put in Tube 8 using the same nickel oxidation recipe (500 °C for 5 hours) to attain ~3500 Å of nickel oxide on the devices.

3.2.1.10 Aluminum – Deposition and Patterning

A 7500 Å thick aluminum film is then sputtered on the wafers (on the PE 4400 sputter tool) as the final electrode. The thickness is confirmed using a profilometric measurement on a test wafer, using Kapton tape as a mask. The wafers then go through Level 5 metal lithography to create the photoresist pattern.

Since the wafers went through the contaminated furnace tube, they cannot be processed in any plasma-etch tool. Therefore, the aluminum film must be wet-etched in the aluminum wet etchant.

The test wafer is then used to measure the etch rate of aluminum in the aluminum wet etchant at ~50 ºC. Using this measured etch rate, Al is then wet-etched off the device wafers. The wafers are then stripped off the remaining photoresist using the standard strip recipe in the wet solvent strip. This concludes the fabrication process.

Upon inspection, it is observed that the aluminum wet etch severely undercuts during etching, especially on topography edges. Several critical areas such as aluminum stepping over ILD SiO_2 show evidence of undercutting. In most areas, the undercutting is not fatal (open-circuit), but some areas of the wafer do show fatal undercutting. Figure 3.12 shows an image of potentially fatal aluminum undercutting near an ILD topography edge.

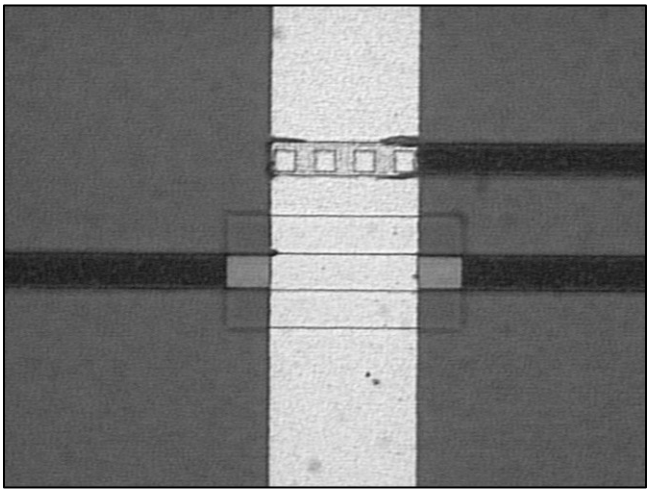

Figure 3.12: Aluminum undercutting over ILD topography edge

Chapter 4

Results and Discussion

As this project investigated two different properties, bolometric and resistive, of nickel oxide, the results for this investigation are separated into two distinct sections – one for the testing results for the nickel oxide microbolometer devices, and the other for the nickel oxide MIM devices. Additionally, the properties of blanket nickel oxide films, created using the same sputter and thermal oxidation processes as those during fabrication, are investigated using ellipsometry, X-ray diffraction studies, tunneling electron microscopy, and energy dispersive X-ray spectroscopy

4.1 Nickel Oxide

4.1.1 Preliminary characterization of nickel oxidation

The thermal oxidation of nickel was conducted at 500 °C for 5 hours. No prior designed experiments were conducted to characterize the oxidation behavior of nickel, partly due to limited time constraints, but also because the thermal oxidation of nickel is not a novel concept. There are many sources of peer-reviewed literature that have experimented with the various process parameters, such as temperature, time, and environment, to characterize the oxidation kinetics of nickel. Therefore, redoing these investigations would have been considered "reinventing the wheel" and it was a reasonable risk taken to

assume that similar behavior should be observed while employing the same process conditions at the RIT SMFL, in the interest of conserving time.

Nickel can be oxidized in several different ways. It undergoes oxidation on its surface even in room conditions. Beyond this, the film must be agitated to grow a thicker nickel oxide film. A nickel oxide film can be achieved through thermal annealing of nickel in an oxygen-rich environment such as a furnace, rapid thermal processing (RTP), using an oxygen plasma, reactively-sputtering nickel oxide during the deposition itself, wet chemical oxidation using wet chemistry, sequential atomic layer deposition to create the film during deposition, and so on. In this project, since the fabrication was mainly limited to the procedure available at the RIT SMFL, many of these options were not possible, such as atomic layer deposition. Also, once formed, nickel oxide can be difficult to selectively etch, barring ion milling. Therefore, another constraint in this project was to deposit a nickel film, pattern it, and then oxidize it to get the required nickel oxide. Also, the rapid thermal processing tool has wafer size restrictions, and is very tricky to use consistently and reliably for a freshly trained user. Therefore, the only two procedures realistically available for use were thermal oxidation and plasma oxidation of sputtered nickel.

During preliminary work for this project, a few test wafers were used to test the plasma and thermal oxidation techniques to see which of the two would provide usable results. The plasma oxidation was preferable, as that would accomplish the additional goal of stripping the sacrificial bridge photoresist as well, thereby combining two critical steps

into one. The sheet resistance of the sputtered nickel film was measured both before and after exposure to an oxygen plasma. Table 4.1 summarizes the results.

Table 4.1: Sheet resistance measurements for plasma oxidation of nickel

Event	Average Sheet Resistance (Ω/sq)
Measurement before exposure to O_2 plasma	0.52
Measurement after exposure to O_2 plasma	0.38

Sheet resistance measurements were taken using the ResMap four-point probe tool. The sheet resistance was observed to *decrease* after a supposed plasma oxidation of the nickel film. This measurement was verified in several locations of several wafers. Surely, any amount of oxidation would result in a highly insulating top film, which, regardless of the conduction path of the current, would result in a high net resistance. This observation was confirmed by Hoey et al. [37] when during their experiment, it was confirmed that plasma oxidation only results in a very small oxidation of the top surface of nickel, around 5-10 nm only. This is because the formed nickel oxide acts as a passive layer, protecting the bulk of the nickel from oxidation. A large power and a very long plasma exposure time is required for any significant amount of oxidation, and even then, 2000 nm of nickel is unlikely to oxidize completely. Their electrical measurements also indicate a decrease in resistivity after plasma oxidation, which is attributed to penetration of the thin oxide by the probes of the instrument. Only one split from their designed showed any increase of resistivity which was from 5.7×10^{-4} Ω cm to 7.91×10^{-4} Ω cm, a

tiny increase and not nearly enough for use in any kind of bolometric or resistive applications.

Thermal oxidation, on the other hand, shows more promising results. D. S. Kim et al. [1] demonstrated feasible nickel oxidation. A 60 nm nickel film was sputtered on several samples, and annealed in an O_2 environment at 310 °C for different soak times for each sample. Each additional hour of annealing showed an increase in resistivity and a change in morphology in conditions. Only after 7.5 hours does the film stabilize. The film's final resistivity is measured to increase by 7 orders of magnitude after a 7.5 hour anneal at 310 °C. X-ray diffraction studies confirmed complete oxidation of the nickel film. The new nickel oxide film thickness measured was 1.69x thicker than the original nickel film – thus confirming and correlating well with the predicted increase demonstrated in Eq. 2.20 – 2.24. Figure 4.1 shows the resistance and thickness increase over time of nickel films treated at 310 °C, as observed by D. S. Kim et al.

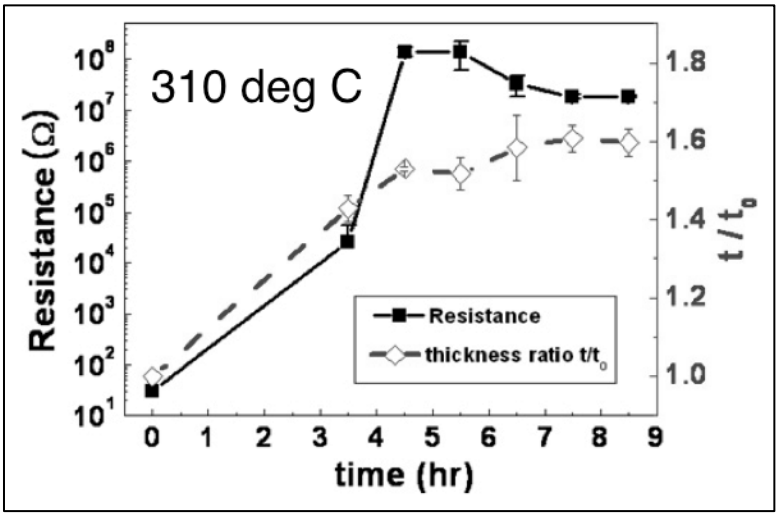

Figure 4.1: Resistance and thickness increase over time of nickel films treated at 310 °C [1]

In this project, the nickel film to be oxidized is on the order of ~200 nm. To compensate for this additional nickel thickness, nickel was instead oxidized at 500 °C for 5 hours in a dry O_2 environment. Initial results were very promising.

The obtained film after thermal oxidation was greenish-yellow in color. The profilometry-measured thickness of the film was 1.6x thicker than the original nickel film. Moreover, the resistivity of the film was too high for the ResMap tool measure. These three facts gave a preliminary indication of the fact that the nickel film was indeed oxidized to form nickel oxide. This process was then used, without change, in the fabrication process.

4.1.2 X-ray diffraction

X-ray diffraction measurements were made on thermally oxidized nickel oxide samples. These measurements were made at the RIT College of Science Condensed Matter Physics laboratory. A sealed tube X-ray source with a θ-2θ diffractometer (the θ arm holds the sample to be measured, and the 2θ arm holds the detector) was used for measurements. The power used for the measurements was ~600 W to keep the source temperature low, and the air environment near the sample was not controlled and therefore air scattering of X-rays is not eliminated. Figure 4.2 shows a picture of the setup of the measurement, which also shows the NiO sample being measured.

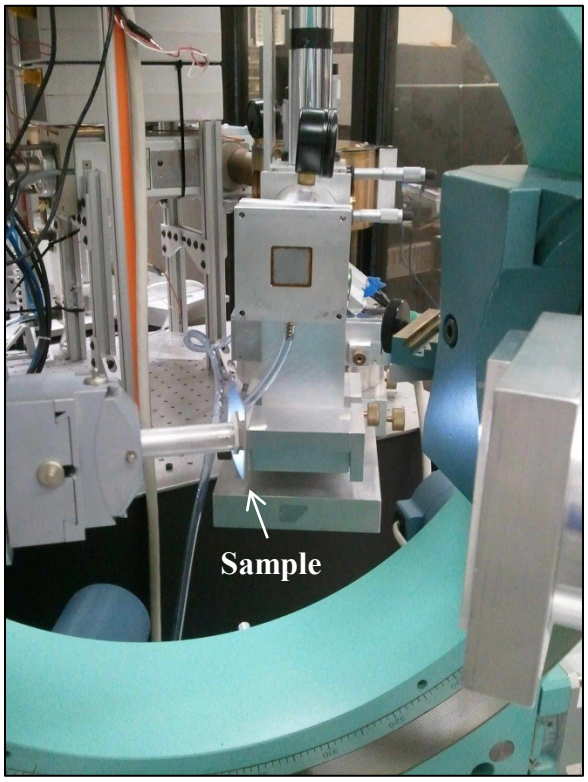

Figure 4.2: XRD Measurement Setup

Cu Kα (λ = 1.54050 Å) X-ray emissions were used for measurements in this study. The Cu refers to a copper source for the Kα X-rays. Kα X-ray emissions result from electron transitions from the 2p orbital of the "L" shell to the innermost "K" shell. Kα is typically by far the strongest X-ray spectral line for an element bombarded with sufficient energy to cause its most intense X-ray emission. Figure 4.3 shows the energy levels and electron transitions involved in Cu Kα and Kβ X-ray emissions.

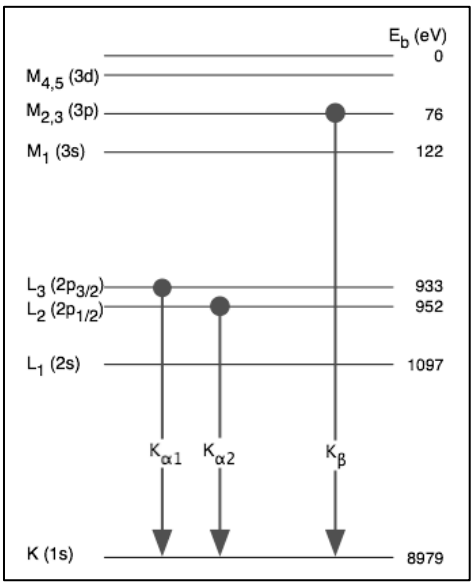

Figure 4.3: Atomic levels and electron transitions involved in Cu Kα and Kβ emission [38]

The initial scan was run from 2θ values ranging from 10° to 60°. The intensity of the constructively interfering reflected X-rays that are in-phase was measured as the number of photons picked up by the diffractometer. Figure 4.4 shows the first scan run on the thermally oxidized nickel oxide sample.

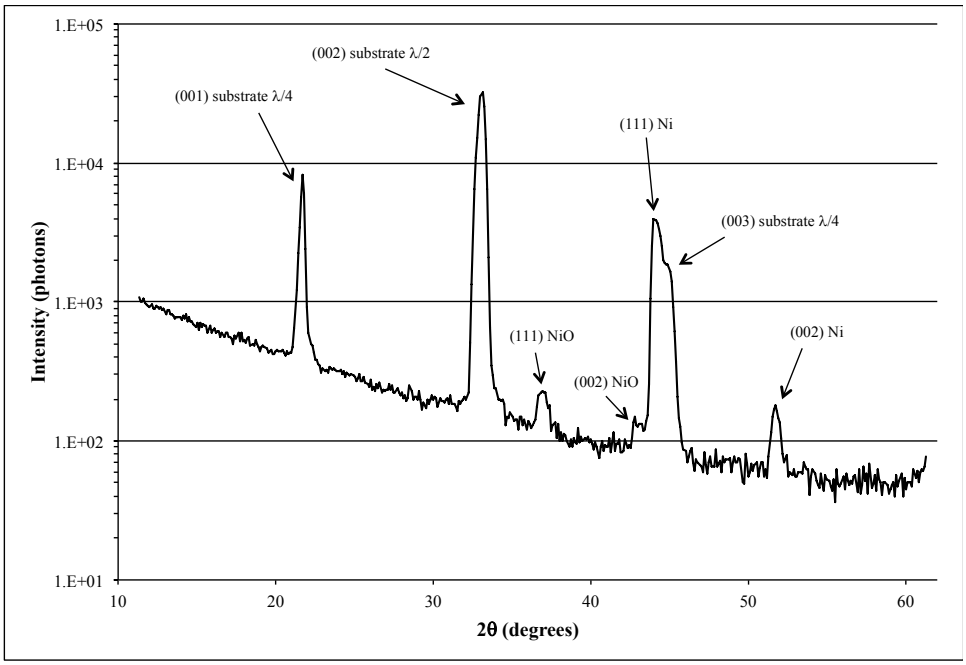

Figure 4.4: Initial large XRD scan of NiO sample

A sample calculation of the miller indices *h*, *k*, *l* of the 2θ=44.3° peak is shown in Eq. 4.1 through 4.2 and Table 4.2.

From, Eq. 2.26 and 2.27: $$\frac{a}{\sqrt{h^2+k^2+l^2}} = \frac{n\lambda}{2\sin\theta}$$ **Eq. 4.1**

where a = 3.524 Å for Ni, λ = 1.54050 Å, θ = 22.15°, and h, k, l, and n are integers. For Ni, which has an FCC structure, h, k, l, must all be even or all odd. Rearranging Eq. 4.1 and plugging in these values, Eq. 4.2 is obtained.

$$\therefore n = \frac{2a\sin\theta}{\lambda\sqrt{h^2+k^2+l^2}} = \frac{2*3.524*\sin\left(22.15^\circ\right)}{1.5405*\sqrt{h^2+k^2+l^2}}$$ **Eq. 4.2**

Therefore, low all odd or all even integer values for *h*, *k*, *l* must be tried until *n* is calculated to be an integer. Table 4.2 shows the calculated values for *n* for various *h*, *k*, *l* combinations.

Table 4.2: Sample XRD calculations to find miller indices

h	***k***	***l***	***n***
0	0	2	0.86
0	2	0	0.86
1	1	1	1.00

Therefore, the miller indices (111) define this crystal lattice of Ni. Similar calculations for the other peaks are performed, using appropriate lattice parameters for NiO.

This initial scan reveals the various major crystal orientations found in the sample. Obviously, the silicon substrate accounts for the majority of the material in the sample, and hence very intense (001), (002), and (003) peaks of silicon (equivalent to [100] silicon) are measured. These all belong to the [100] crystal orientation of the silicon lattice, the difference only being due to different naming conventions between crystallographers and physicists. Due to these sharp substrate peaks, other peaks appear smaller in comparison, but are still clearly visible. The (111) and (002) orientations for both Ni and NiO are measured. This is indicative of polycrystalline grains of both Ni and NiO in the film. It also indicates significant but incomplete oxidation of the Ni.

Another XRD scan was conducted on the same sample to better observe these Ni and NiO peaks. This time, a smaller range of 2θ is measured (only 34° to 48°), the slits are narrowed a bit and theta is offset by 0.5° to reduce the higher order lambda (substrate) reflections from contributing to the measurement. Figure 4.5 shows this second XRD scan's results.

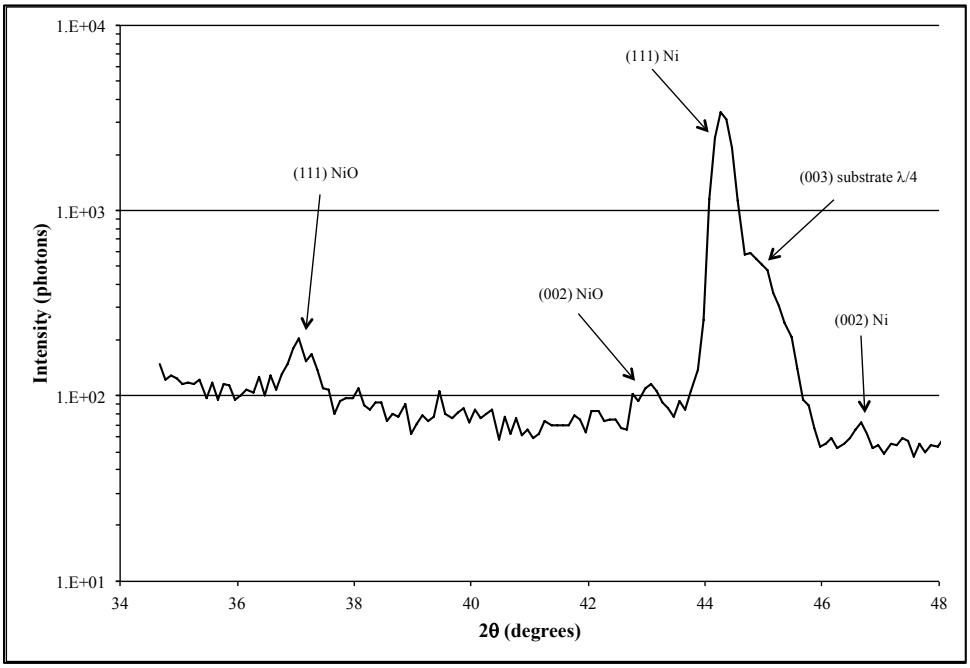

Figure 4.5: Second XRD scan of NiO sample

This second scan was run much faster than the initial one, and therefore the noise floor is higher. This tilted scan significantly reduces the (003) substrate peak intensity from $2x10^3$ photons to $5x10^2$ photons, thus allowing better observation of the Ni and NiO peaks. This scan clearly shows the (111) and (002) peaks of both Ni and NiO. Since the (111) peaks of both Ni and NiO and respectively higher than their (002) peaks, it is likely

that a significant majority of the nickel from retained its crystal structure after it was oxidized. This scan also confirms that a significant amount of nickel remains non-oxidized, further confirming the passive protection properties of nickel oxide film.

4.1.3 Ellipsometry

Ellipsometric measurements were conducted on blanket nickel oxide grown on the silicon substrates. The film stack in study is depicted in Figure 4.6.

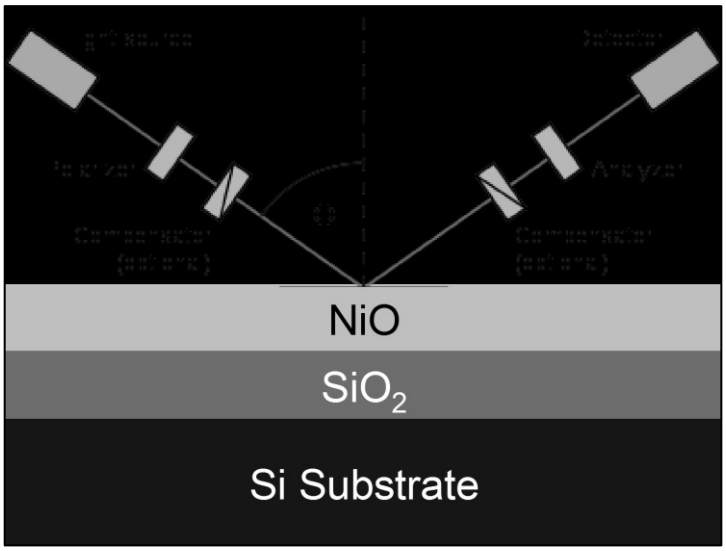

Figure 4.6: Film stack for ellipsometry study

The film stack being tested is a very non-uniform, non-transparent, complex film stack. As evidenced from the XRD studies, the NiO film has several crystal orientations within it, along with residual non-oxidized Ni. Therefore, a single angle, single wavelength ellipsometric measurement will not provide exact Δ and Ψ values that can be used for calculating the complex refractive index for the NiO film. Nevertheless, the K value

(imaginary component of the complex refractive index) extracted, while not precise, can still provide information about the absorption of a sample for a particular wavelength. In this case, high absorption tendencies of NiO are desired in the infrared spectrum.

Therefore, a wavelength of 830 nm, deep into the infrared, is used for an ellipsometric measurement. The Δ and Ψ parameters measured are shown in Eq. 4.3, and the calculated N_S and K_S parameters (as per Eq. 2.28) are shown in Eq. 4.4.

$$\Delta = 138.45 \quad \Psi = 11.58 \qquad \textbf{Eq. 4.3}$$

$$N_S = 3.484 \quad K_S = 0.921 \qquad \textbf{Eq. 4.4}$$

Here, the extracted K_S value calculated is 0.92, which is indicative of a very high infrared absorption film. This kind of absorption is necessary and appropriate for bolometric applications, and confirms the viability of nickel oxide for such purposes.

To conduct further ellipsometric analyses of NiO, a simpler film stack needs to be created. Therefore, 4 Corning EAGLE 2000 4" quartz wafers are obtained. Nickel is sputtered on them and they are put in the furnace for different soak times each. Table 4.3 summarizes the splits.

Table 4.3: Design of NiO ellipsometry experiment

Wafer	Soak Time in dry O_2 at 500 °C
1	1 hour
2	2.5 hours
3	4 hours
4	5 hours

During this soak time experiment, the wafer boat loader encounters an error and wafer 3 is not correctly oxidized; it is therefore scrapped from the experiment. The other wafers are oxidized according to their respective soak times. After oxidation, all three wafers show an equally green translucent film on the transparent quartz substrates. However, the adhesion of this film to the substrate is very poor and it begins to flake off the wafers. Figure 4.7 displays a photograph showing the NiO de-adhesion.

Figure 4.7: NiO de-adhesion from quartz substrates

After consulting some Corning engineers who provided the wafers, it is hypothesized that the quartz wafers provided may have expanded and/or shrunk as part of the thermal ramp up and ramp down involved in the furnace step. A mismatch of coefficient of thermal expansion between the Ni/NiO film and the quartz substrates led to a lot of stress that caused the film de-adhesion. For future attempts at this experiment, a pre-compaction anneal of the quartz substrates is recommended to thermally exercise the substrate. Very slow ramp up and ramp down steps are recommended for these substrates.

Obviously, ellipsometric measurements on the fabricated NiO films on quartz substrates are now impossible. Yet, the ellipsometric measurements of NiO films did yield a significantly importantly conclusion that NiO is highly absorbing in the infrared range of the electromagnetic spectrum. This is crucial to the success of NiO for use as a microbolometric sensitive material.

4.1.4 Transmission Electron Microscopy & Energy Dispersive X-ray Spectroscopy

Transmission electron microscopy (TEM) and energy dispersive X-ray spectroscopy (EDS) is conducted on several samples of thermally oxidized and plasma oxidized nickel oxide samples. A few samples of the final fabricated dies were also sent for the imaging of the microbolometers and MIM devices. These samples were sent to the Failure Analysis team at Micron Technology Inc., where these studies were conducted. Both Z-contrast and bright field images were obtained as part of the study.

Blanket plasma oxidized and thermally oxidized samples of nickel oxide on SiO_2 on Si substrate were analyzed using this technique. The goal of this exercise was to investigate and compare the cross-section profiles of the grown nickel oxide films. Figure 4.8 shows the Z-contrast and bright field images of the plasma oxidized nickel oxide film respectively.

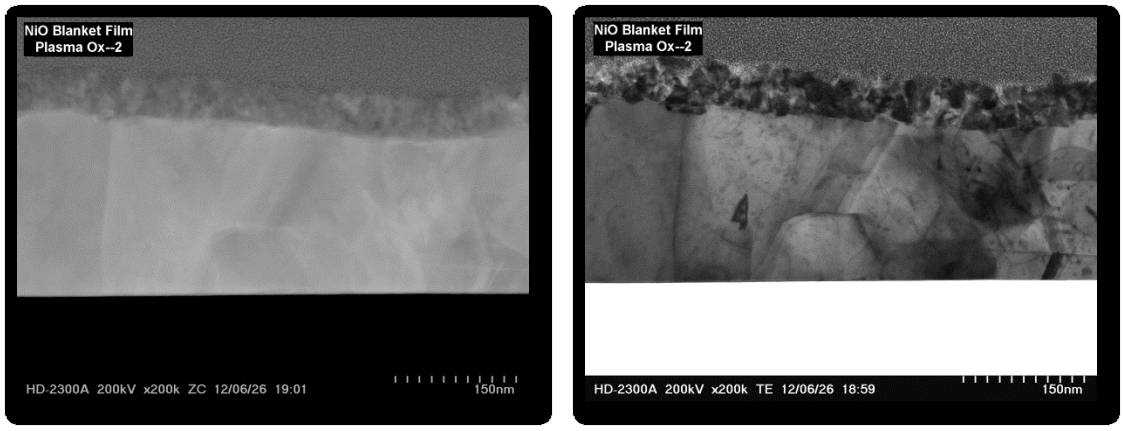

Figure 4.8: Z-contrast and bright field TEM images of plasma oxidized NiO sample

From Figure 4.8, it is clear that there is some sort of thin top surface cloudy above a thicker, more granular, and polycrystalline film, which, in turn, lies on top of a uniform amorphous film. It is not indicated what elements make up each of the films, and this is where EDS provides these answers. Figure 4.9 below the EDS analysis of this film stack.

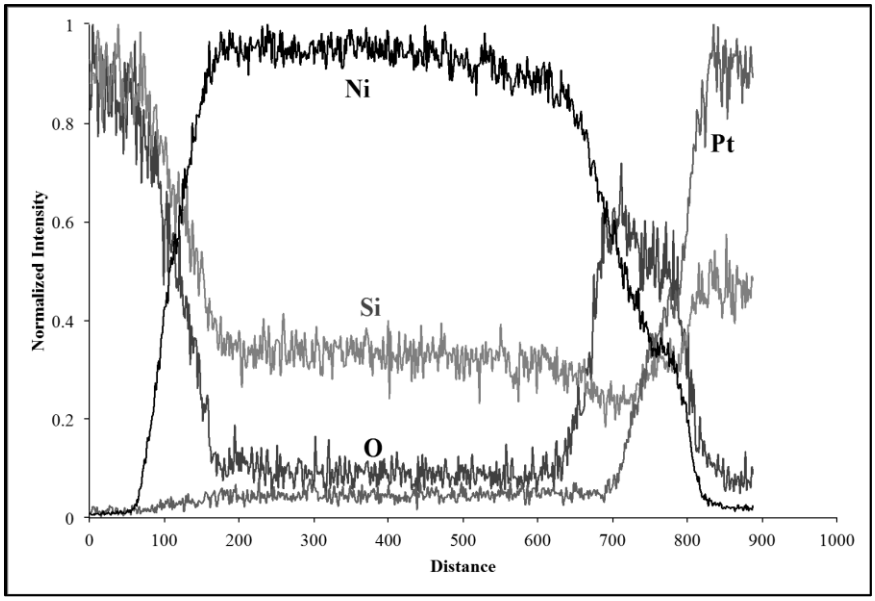

Figure 4.9: EDS results for plasma NiO sample

The graph above represents the normalized intensities of the particular elements as they appear in a cross-section measurement. Therefore, the x-axis in Figure 4.9 matches the vertical cross-section of the images shown in Figure 4.8 with x=0 corresponding to the bottom of the TEM image. Therefore, if one were to superimpose the two, the EDS graph would have to be effectively rotated 90° counter-clockwise.

The relative normalized intensities of Ni and O as shown in Figure 4.9, along with the TEM scans from Figure 4.8, together indicate that the thicker, granular, polycrystalline

film in the middle is most just Ni metal which has not been oxidized. To its right, a thin region with higher O concentration and a lower concentration of Ni is observed, which corresponds to the cloudy top-surface region in the TEM. This can therefore be deduced to be the plasma oxidized NiO film. To its right is a region with much higher Pt content, which is the Pt cap used to protect this region of interest (ROI) during FIB milling as part of sample preparation for TEM. All the way to the left is a region with Si and O concentration, which respectively corresponds to the amorphous thick film at the bottom of the TEM, and is therefore deduced to be SiO_2. From the TEM image, it is clear that the NiO film is roughly ¼ of the thickness as the rest of the Ni metal film. Therefore, its thickness is in the proximity of ~50 nm only.

Therefore, it is clear that plasma oxidation only results in the oxidation of the top ~50 nm of the nickel metal. This confirms the hypothesis made during preliminary analysis of the project when plasma nickel oxidation resulted in a decreased sheet resistance.

Figure 4.10 shows the Z-contrast and bright field TEM images for a thermally oxidized nickel oxide sample.

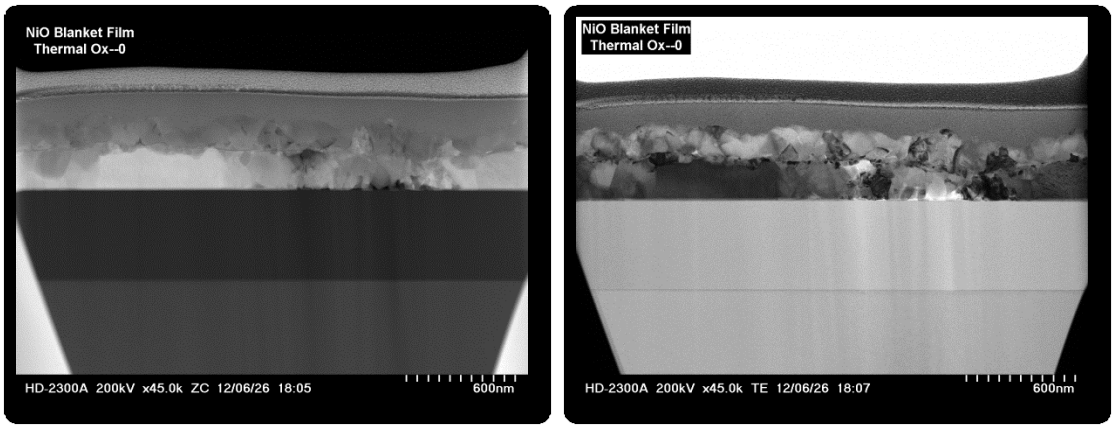

Figure 4.10: Z-contrast and bright field TEM images of a thermally oxidized NiO sample

From Figure 4.10, the top thin film is the Pt cap. A dark, granular, cloudy film is observed above a slightly thicker, lighter in shade, granular, polycrystalline film. This, in turn, lays on top of a thick, uniform, amorphous film. Figure 4.11 shows the EDS analysis of this film stack.

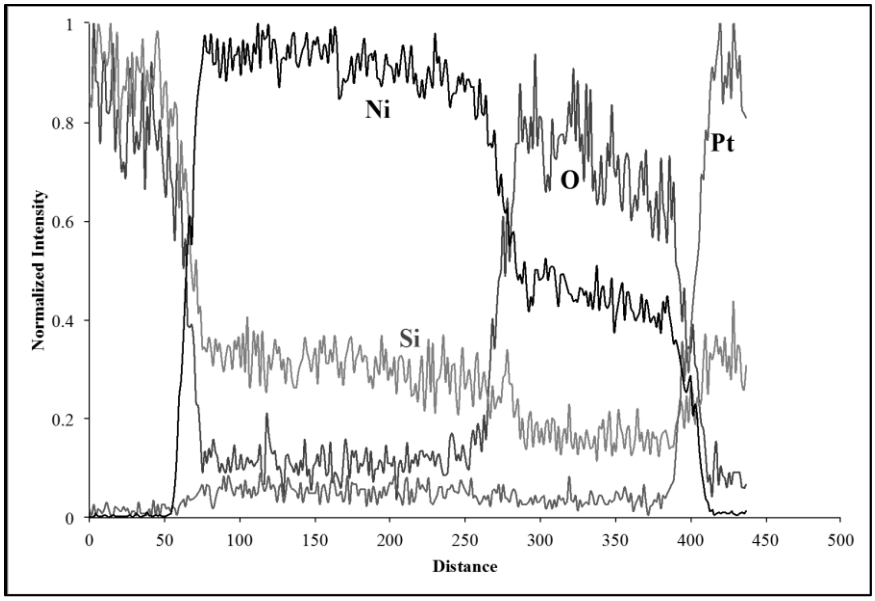

Figure 4.11: EDS results for thermally oxidized NiO sample

To the far left of the graph, only Si and O have high concentrations, indicating that this is the thick, uniform, amorphous SiO_2. To its right is a region with high concentration of Ni only, indicating that this is the Ni metal region that has not been oxidized. This corresponds to the lighter in shade, granular, polycrystalline film from the TEM images. To its right is a region with lower Ni concentration but high O concentration, indicating that is the thermally oxidized NiO film. This corresponds to the dark, granular, cloudy film from the TEM images. To its right is a region with Pt, which is the Pt protective cap.

From both the TEM images and EDS graphs, it is calculated that the NiO film is about 65% of the thickness as the rest of the Ni metal film, much higher than plasma oxidation. This corroborates with the XRD results as well that indicated that a significant amount of Ni was left un-oxidized.

4.1.5 Nickel oxidation modeling

Now that the actual nickel oxide thickness is measured, model parameters for nickel oxidation can be extracted. If z is defined as the NiO thickness, x is defined as the Ni consumed during NiO growth, and y is defined as the Ni remaining to be oxidized, Eq. 4.5 can show their relationships based on the predicted film expansion due to oxidation from Eq. 2.24, and the known initial nickel deposition thickness of 210 nm.

$$z = 1.699x \quad \& \quad y = 210 - x \qquad \textbf{Eq. 4.5}$$

Now, from the TEM/EDS analysis, the thickness of the nickel oxide film was measured to be approximately 65% that of the un-oxidized nickel film underneath.

$$\therefore \frac{z}{y} = \frac{1.699x}{210 - x} = 0.65 \square \quad x = 130\ nm \qquad \textbf{Eq. 4.6}$$

The process conditions for this thermal oxidation were as follows: temperature was 500 °C (or 773 K) and soak time was 5 hours (or 18,000 seconds). Using these values, along with the necessary constants and tabulated values of ΔH and ΔS from Table 2.2, in Eq. 2.10 yields a nickel consumption of ~120 nm, assuming no native nickel oxide. This calculated value of nickel consumption is very close to the extracted nickel consumption value from TEM/EDS analysis. This confirms that the thermal oxidation of nickel does indeed follow very closely with the predicted oxidation kinetics based on enthalpy and entropy of activation. More data is needed in order to verify if nickel oxidation follows the parabolic law (Deal and Grove model).

4.2 NiO Microbolometers

4.2.1 Electrical Testing

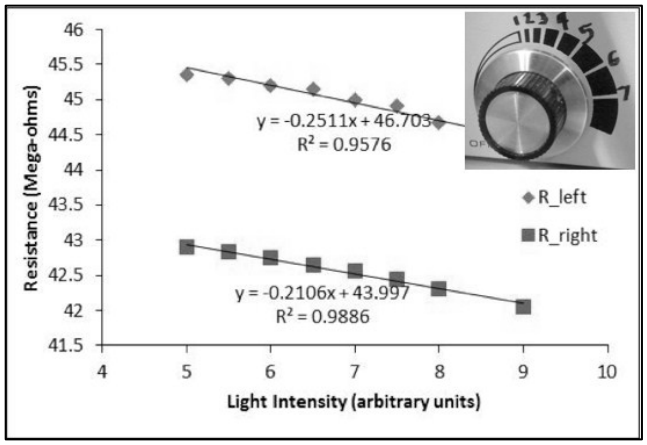

Figure 4.12: Change in resistance of pixel resistors vs. light intensity (analog dial pictured)

The resistors in the sixteen pixel arrays were manually probed and connected to a digital ohmmeter. A light probe with an analog intensity dial was used to heat up the resistors. The resistors, measured 43 MΩ at room temperature, went down to 42 MΩ when measured at full light intensity, as shown in Figure 4.12. A diode circuit (Figure 2.11) was used to measure the temperature increase when switching the light to full intensity. The diode on-voltage at V_O decreased by 23 mV, which, assuming a temperature dependence of -2.2 mV/ºC, corresponds to a ~10ºC increase. Thus, the calculated TCR is TCR of -0.23%/°C. The expected TCR is -3.3%/°C. The difference between the two can be explained due to the fact of incomplete oxidation of the nickel leaving a film of Ni parallel to the NiO which reduces the absorption of the infrared radiation.

However, the problem with this measurement is the lack of proof that the change in resistance was indeed caused by infrared absorption versus visible light absorption. Therefore, a similar test is conducted using an infrared LED as the source of the infrared light. Figure 4.13 shows a picture of the setup during this testing, showing the infrared LED.

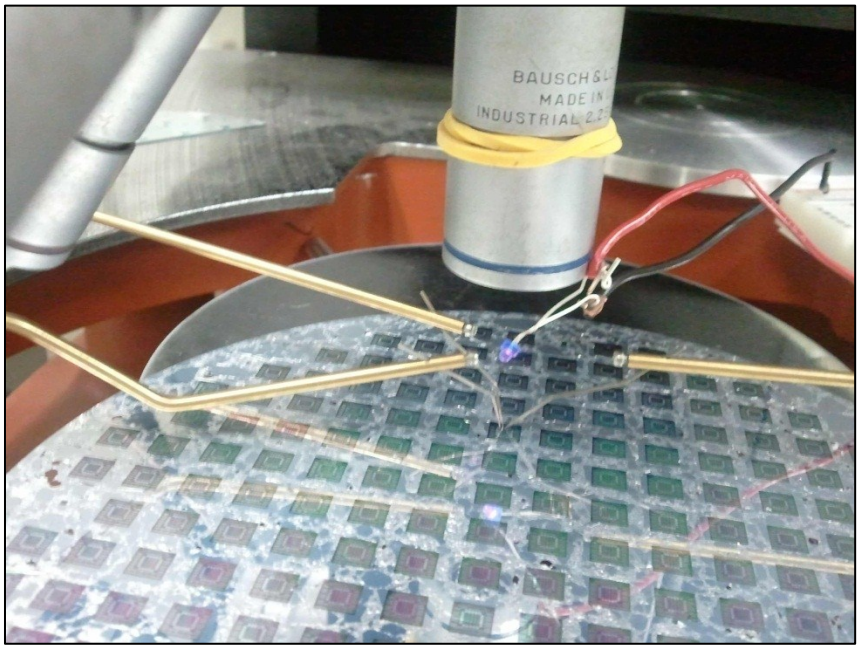

Figure 4.13: IR LED microbolometer electrical testing

The voltage readout through the voltage divider circuit (refer to Figure 3.1) is measured before and after the LED is turned on. Figure 4.14 shows this data collected.

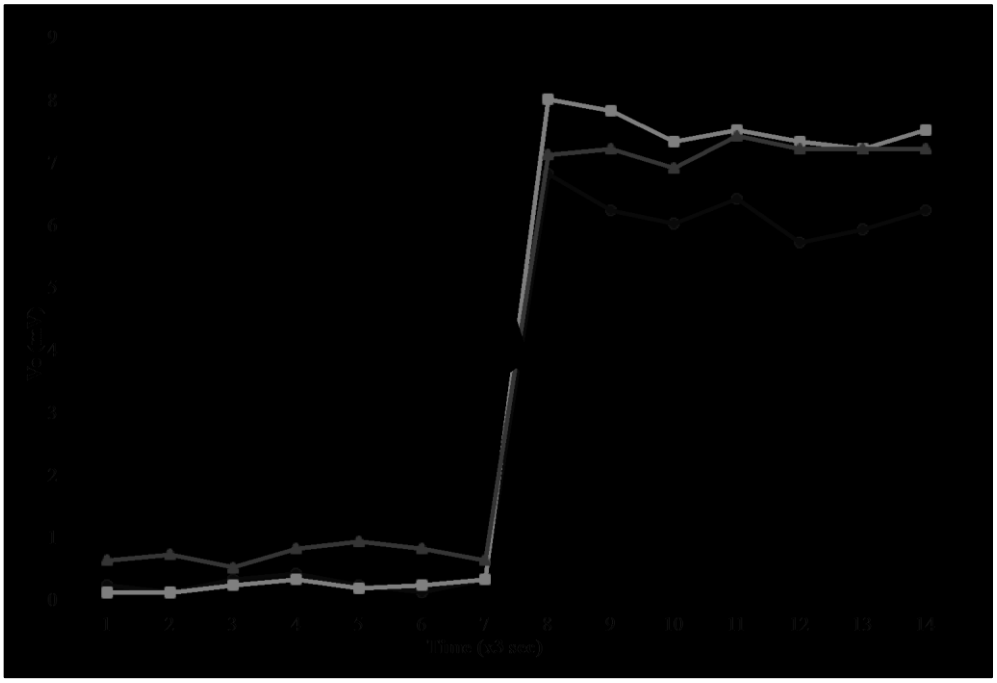

Figure 4.14: Voltage divider output voltage over time as IR LED is switched on

The star represents the time at which the infrared LED is turned on. The different lines represent different resistors measured using this technique. For each resistor, as soon as the infrared LED is switched on, the voltage readout from the voltage divider circuit of the microbolometer pixel goes from ~0 mV to over 6 mV. This is a clear signal that can easily be amplified and used as a temperature sensor.

4.3 NiO MIM Devices

4.3.1 Electrical Testing

The NiO MIM devices were tested to investigate their resistive properties. Electrical testing was done using the HP 4145B Semiconductor Parameter Analyzer. Two major kinds of electrical tests – current vs. voltage (I-V) and current vs. time (I-t) – were performed.

Most resistive switching devices exhibit a change in resistive state when a particular threshold voltage is reached. Figure 4.15 shows a common kind of resistive switching behavior observed in Pt/NiO/Pt MIM structures.

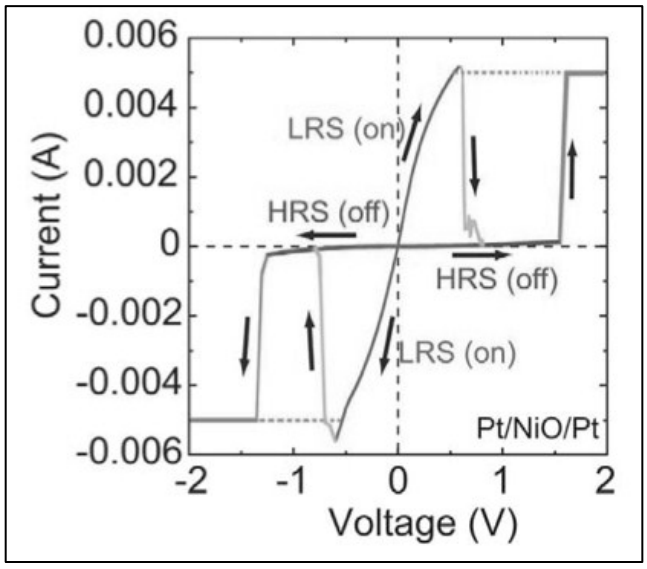

Figure 4.15: I-V curve showing unipolar resistive switching [3]

Here, a thermo-chemical switching mechanism is proposed whereby a thin filament conducts current in a low resistive state (LRS) until a sufficiently high current is passing that breaks (fuses) the filament (which is called a "reset"), thereby resulting in a high resistive state (HRS). The device can be "set" again to the LRS by applying a threshold voltage higher than the reset voltage to reform the filament. This is called unipolar switching as switching depends on the amplitude of the voltage applied, but not the polarity. [3]

Bipolar resistive switching shows directional switching based on the polarity of the voltage applied. This kind of switching is common among transition metal oxides. Figure 4.16 shows a current-voltage curve showing bipolar resistive switching.

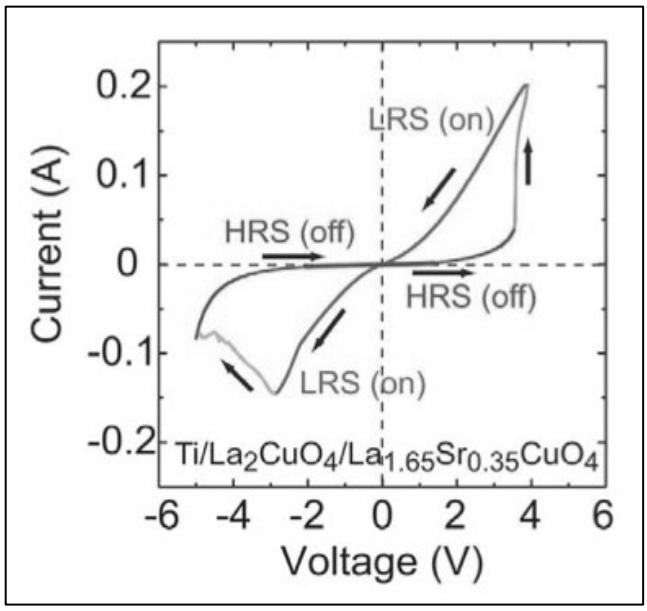

Figure 4.16: I-V curve showing bipolar resistive switching [3]

In bipolar switching, the resistive switching characteristics depend on the electronic properties near the interface of the metal electrode and the oxide. The contact resistance between the metal electrode and the oxide changes upon the application of an electric field. Several models have been proposed to explain this behavior, such as the presence and electromigration of oxygen vacancies, trapping of charge carriers, etc. The change in slope of the I-V curve depending on the direction of the voltage sweep is often referred to as hysteresis. This kind of resistive switching is not commonly observed for NiO.

In this study, the MIM structures, during a current-voltage sweep from -5 V to +5 V, did not show evidence of unipolar or bipolar resistive switching, as is shown in Figure 4.17.

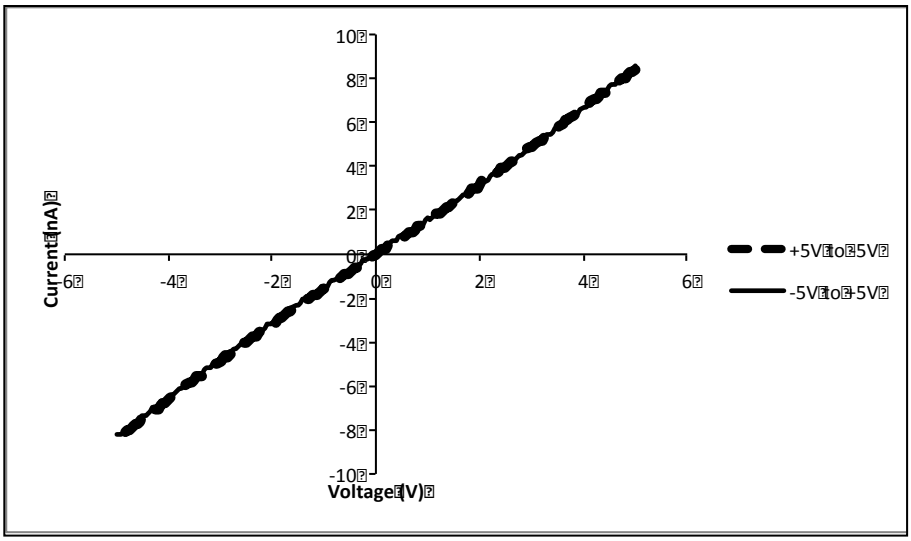

Figure 4.17: I-V curve showing no unipolar or bipolar switching on a 5 μm device

There is no specific voltage at which the resistance state abruptly switches from LRS to HRS or vice versa, and the slope of the curve does not change based on direction of

voltage sweep. In fact, the I-V is very smooth and linear, seemingly indicative of a normal resistive film. This is very undesirable for typical resistive memory applications.

A second kind of electrical testing was conducted to observe the current flow through the device when a constant voltage of 5 V is applied to it for a longer time. The results of this test are shown in Figures 4.18 – 4.21.

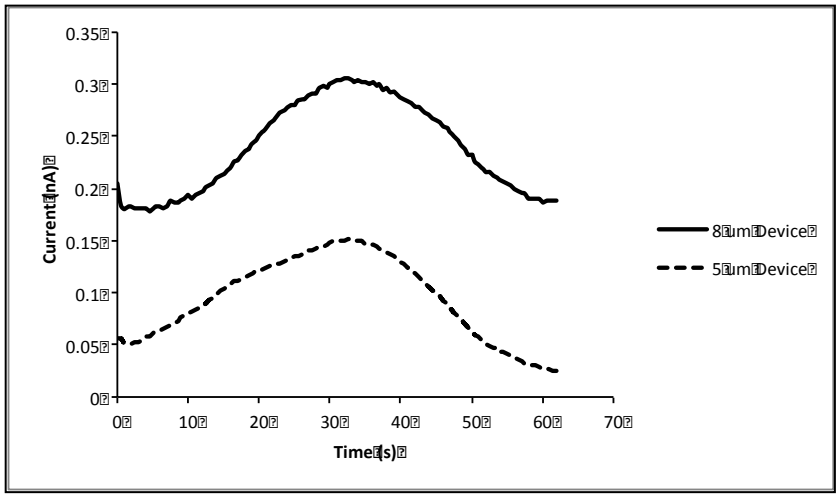

Figure 4.18: Current vs. Time at 5 V for 5 µm and 8 µm MIM devices (60 s)

A very interesting result is obtained when a constant voltage bias is applied across the NiO MIM device. The current flow seems to smoothly rise to a maximum and go back down. Figure 4.19 shows the result when the measurement time is increased to 3 minutes.

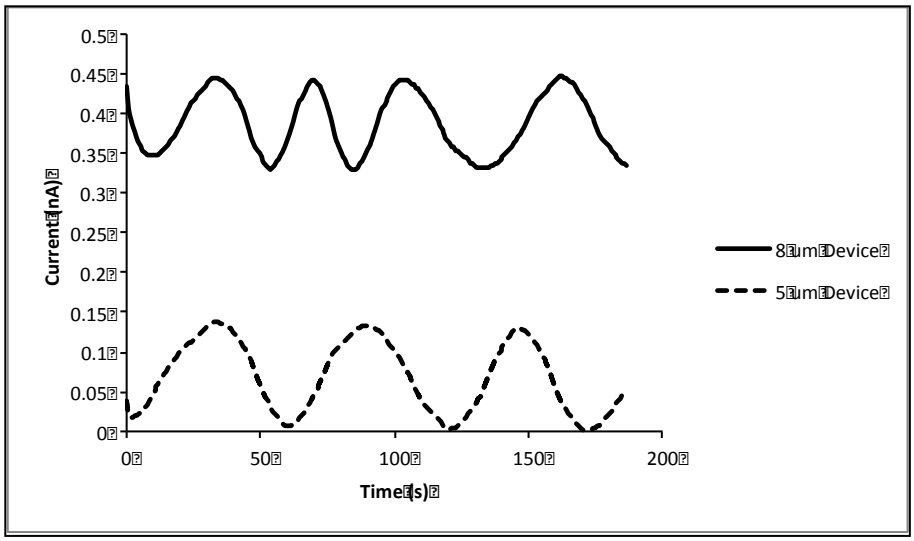

Figure 4.19: Current vs. Time at 5 V for 5 µm and 8 µm MIM devices (180 s)

When the same constant voltage test is conducted for 3 minutes continuously, an repeating oscillating current pattern, albeit with a very low frequency, is observed. Correspondingly, it can be said that the resistance of the film also oscillates slowly between a low-resistance state (LRS) and a high-resistance state (HRS) when placed under a constant voltage bias of 5 V. A new type of resistive switching, one that results in stable, repetitive, and uniform current oscillations at a very low frequency when a fixed voltage bias is applied, is observed.

To confirm that is not a tester artifact, diffused 400 µm x 40 µm resistors are also tested at the same test settings. Figure 4.20 shows the I-t plot for a diffused resistor.

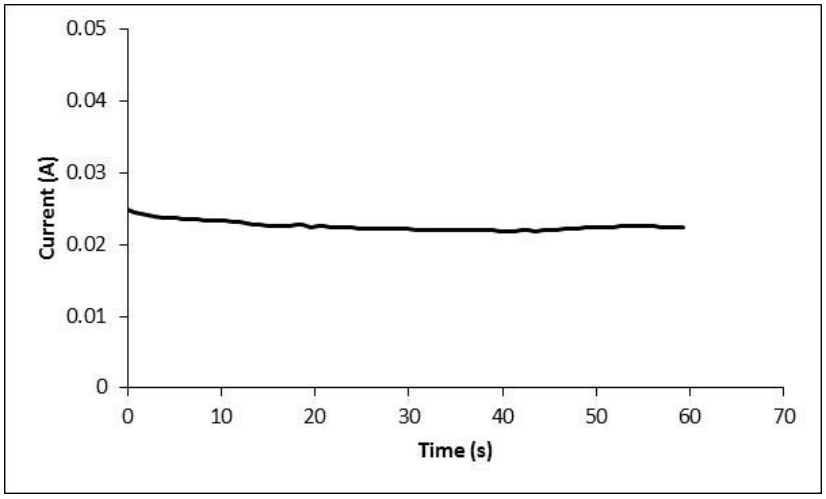

Figure 4.20: Current vs. Time at 5 V for a diffused resistor

The diffused resistor does not show a varying current profile over time. The current stays very uniform and the resistor behaves quite close how an ideal resistor would perform, with no switching in resistive states. It is thus confirmed that the resistive state oscillation observed for the MIM devices is not a tester artifact.

To characterize this new resistive switching mechanism, similar testing is done for various sizes of devices, ranging from 1 μm devices to 10 μm devices, and at various bias voltages. Figure 4.21 shows an I-t plot for different 5 μm square MIM devices, measured at different voltages each.

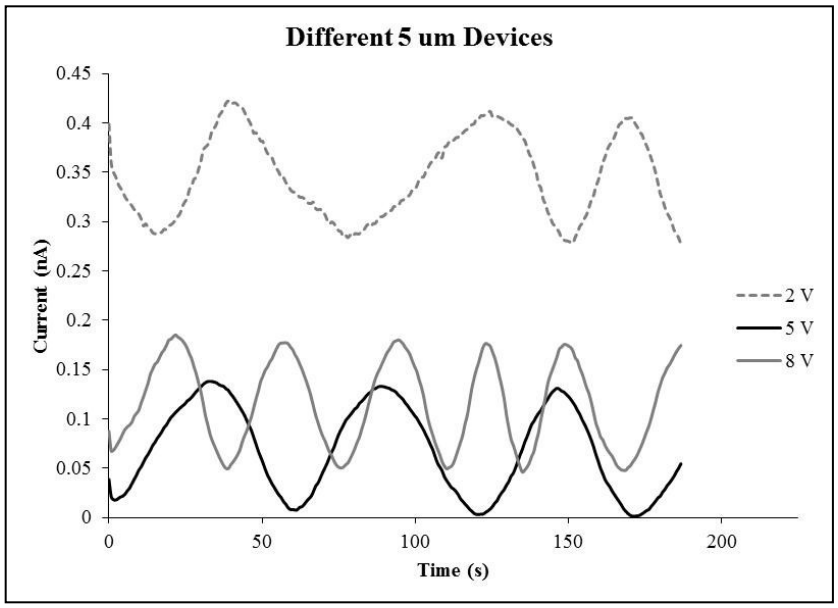

Figure 4.21: Current vs. Time at different voltages for 5 μm MIM devices

Figure 4.21 shows the current vs. time measurement for 3 different 5 μm MIM devices measured at 2 V, 5 V, and 8 V respectively. The frequency of the resistive state switching and the high current to low current ratio (high-low ratio) of the devices is seen to change based on the measurement voltage. The DC shift between the measurements is not intelligible due to low yield and variation between die caused by various process complications (such as aluminum undercutting, tantalum oxidation, etc.). Several such tests are conducted on different sizes of the MIM devices to observe trends due to change in voltage bias.

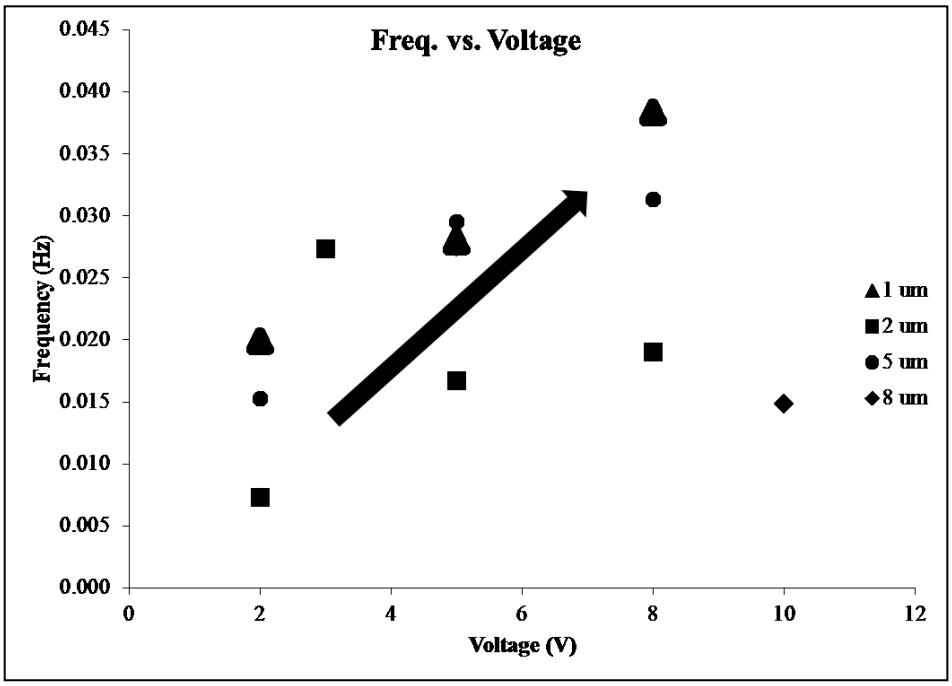

Figure 4.22: Switching frequency for different voltages for various sizes of MIM devices

Figure 4.22 shows a summary of the resistive state switching frequency measured for various sizes of MIM devices measured at different voltage biases. The general trend seems to indicate that an increase in in voltage bias would result in an increase in resistive state switching frequency. This observation leads to a theory for the resistance switching mechanism. This theory is a slightly modified version of the unipolar resistance switching commonly observed.

The theory behind this modified unipolar resistive switching for nickel oxide is still based around the idea of repetitive forming and destruction of thin filament conduction paths. These filament conduction paths form, potentially at grain boundaries, or film edges, or due to migration of nickel atoms in the nickel oxide film, due to an electric field across

the oxide as per to the voltage bias applied. This electric field causes several filaments to be formed sequentially. Once a filament is formed, it starts conducting a higher amount of current. This increased current flow through thin filaments causes them to start heating up due to dissipate the power and eventually, once a certain threshold temperature is reached, break. The filaments that form earlier also break earlier, which is why a sharp transition is not observed. The continued applied voltage causes them to subsequently reform and then fuse again, and so on.

It therefore makes sense that a higher applied voltage bias, and thus higher electric field, would speed up this entire process of formation and destruction of the thin conducting filaments, thereby increasing the resistive state switching frequency.

The high-low ratio is the ratio of the maxima and minima of the current profile over time for a resistive switching film. The high-low ratio is essentially equivalent to the contrast between the LRS and HRS of the material. A high-low ratio close to 1 is indicative of no resistance state switching over time. Therefore, an ideal resistor would have a high-low ratio of exactly 1.0. The diffused resistor shown in Figure 4.20 has a high-low ratio of only 1.03, indicating a non-switching device.

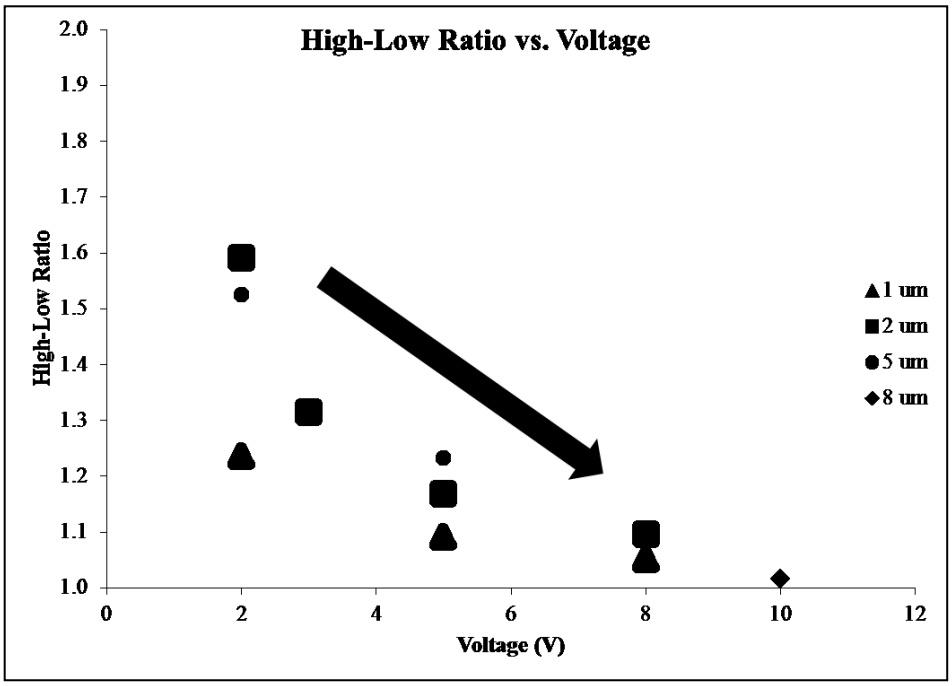

Figure 4.23: High-low ratio for different voltages for various sizes of MIM devices

Figure 4.23 shows a summary of the various high-low ratios extracted from current vs. time measurements for different sizes of MIM devices at different voltage biases. As explained by Figure 4.22, a higher voltage bias leads to a higher switching frequency. The general trend from Figure 4.23 seems to indicate that an increase in in voltage bias would result in a decrease in high-low ratio of the device. This also makes sense because a higher frequency of switching would allow lesser time for the thin conducting filaments to stay broken before they are reformed. Thus, the low current of the devices is not allowed to reach that low. A high high-low ratio is desirable to increase the contrast between the LRS and HRS. Therefore, a trade-off between the switching frequency and high-low ratio is observed, and an operation point that optimizes both of these must be chosen, based on device's intended use.

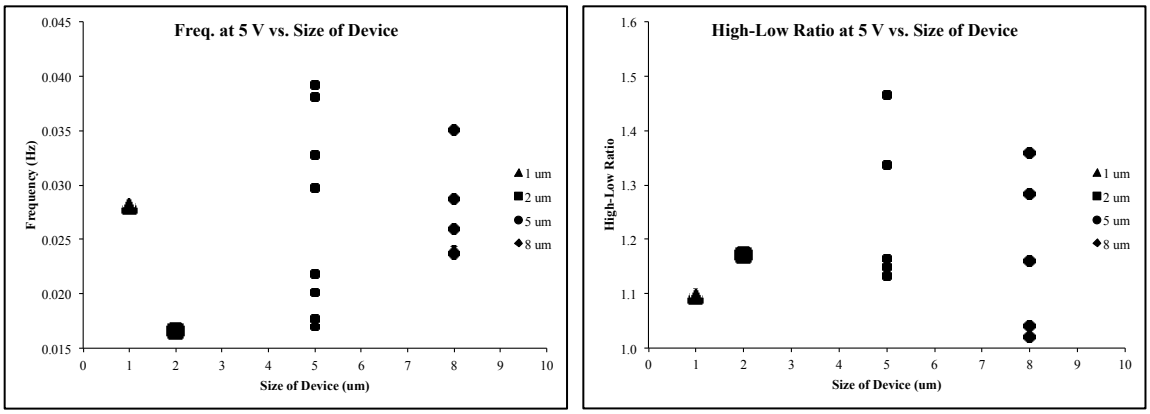

Figure 4.24: Frequency of switching and High-Low Ratio vs. MIM Device Size

Figure 4.24 shows the frequency of resistive switching and the high-low ratio of various sizes of MIM structures. No clear trend is observed for the various dimensions of areas, which additionally corroborates the idea that the current is not flowing through the complete area of the film, but rather through thin conducting filaments, and hence it would not scale with area.

In order for this switching mechanism to function for a resistive memory device, the resistive state must be retained even after the voltage bias is switched off. To check this phenomenon, a 5 μm MIM device is stressed at 5 V and the voltage is switched off at the low resistance state. Figure 4.25 shows the I-t plot and Figure 4.26 shows the I-V graph immediately after the stressing.

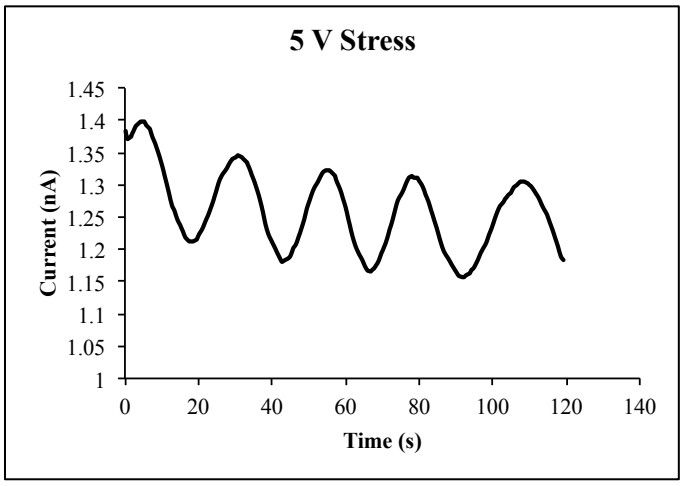

Figure 4.25: 5 V stressing of a 5 μm MIM device, stopped at LRS

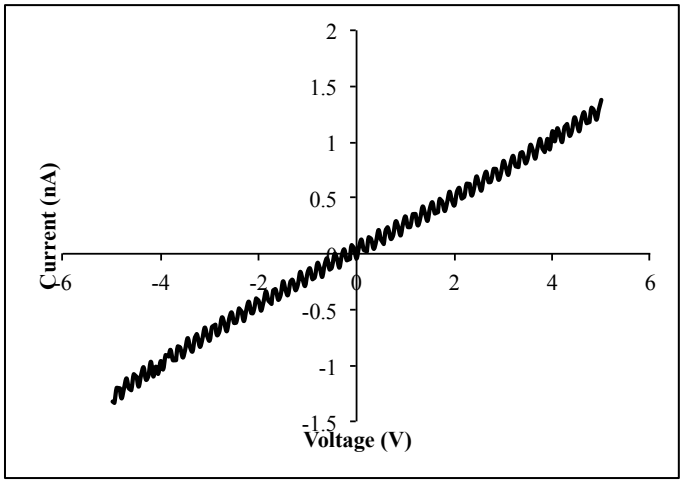

Figure 4.26: I-V curve measured immediately after 5 V stressing stopped at a LRS

The initial current measured in the I-t measurement is ~1.38 nA. The LRS state measures a current of ~1.2 nA. The I-V curve shows the current level measured at a voltage of 5 V being ~1.37 nA. Therefore, it appears as though the device reverts back to its original state once the voltage stressing is stopped, and does not retain its current resistive state.

Forcing a specific level of current and measuring voltage is also attempted; however, the measured voltage does not show any oscillations, indicating that this resistive switching mechanism is driven by a constant electric field across the oxide. Figure 4.27 shows the results of constant current testing.

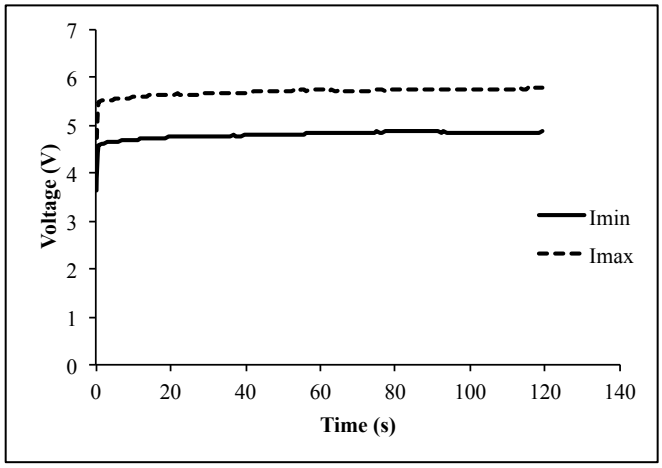

Figure 4.27: Voltage vs. time for constant current testing

TEM/EDS analysis was also conducted on MIM structures. The desired film stack is Ta/NiO/Al. Figure 4.28 shows the TEM image and Figure 4.29 shows its EDS analysis.

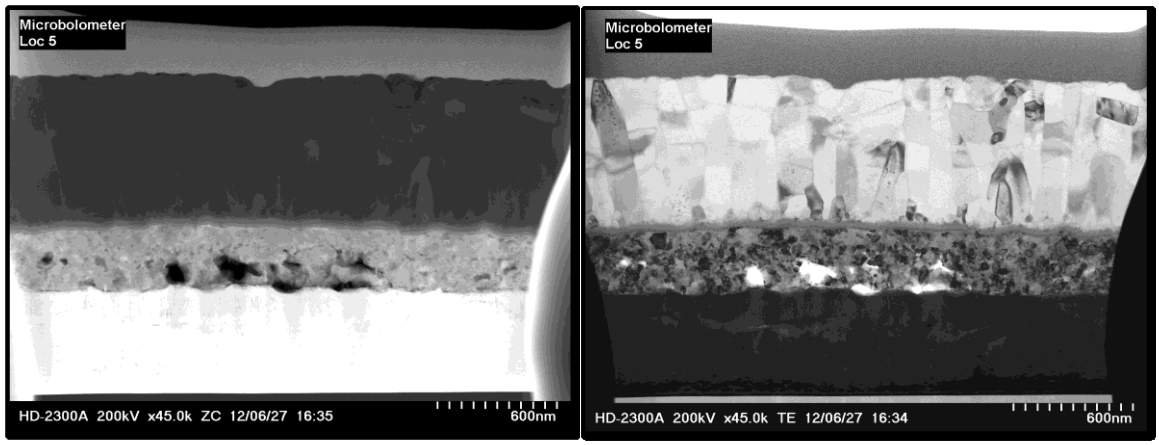

Figure 4.28: TEM Z-contrast and bright field images of an MIM device

The top of the TEM image is the Pt cap. Below it is a dark, thick film with long columnar grains. Below it is a lighter, granular, cloudy, film. Below it is a light, polycrystalline for which, the bright field image shows the bottom edge of it being darker than the rest. EDS analysis helps identify each of the films.

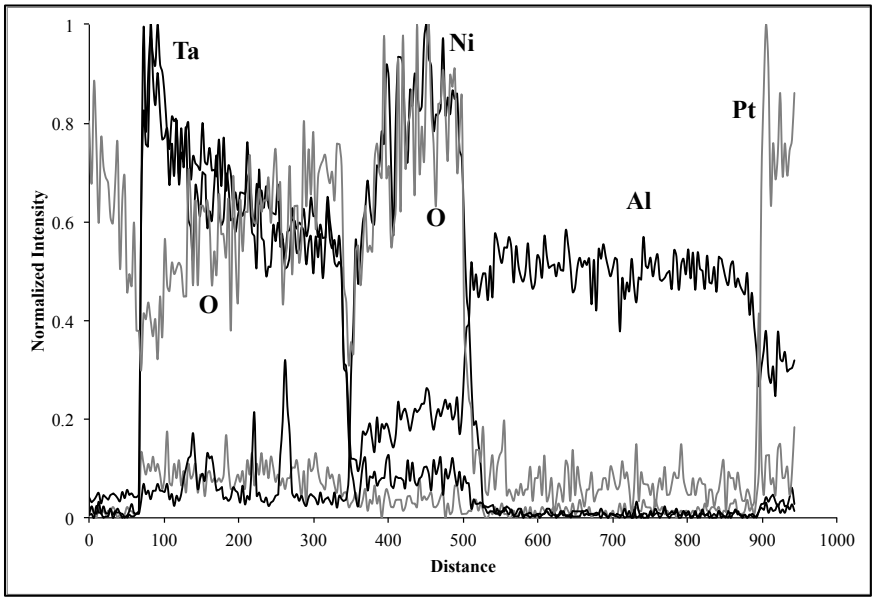

Figure 4.29: EDS analysis of the MIM device

EDS analysis shows the far right film being the Pt cap. To its left, is Al, which corresponds to the long, columnar grains from the TEM. To its left is a completely oxidized NiO film, which is the dark, grainy, cloudy film in the TEM. To its left, is a film with high concentrations of Ta and O, indicating that this is a significantly oxidized Ta_2O_5 film. The left portion of this film has lesser O than the rest, indicating that this is the residual Ta remaining un-oxidized. Therefore, the Ta film has been significantly oxidized and so has the Ni film to form nickel oxide. Both of these contribute to the MIM's resistive properties observed through its electrical testing, which makes it difficult to separate the Ta_2O_5 film's conduction mechanics from the NiO conduction mechanics.

Chapter 5

Conclusions

Nickel was successfully oxidized through a furnace thermal oxidation process, involving a 500 °C soak in dry O_2 for 5 hours. Through various means of characterization, the bolometric and resistive properties of nickel oxide have been investigated. In addition, attempts have been made to model nickel's thermal oxidation based on tabulated enthalpy and entropy of activation parameters. Physical thickness measurements using profilometry, ellipsometry, and materials analysis using x-ray diffraction, transmission electron microscopy, and energy dispersive spectrometry, and electrical measurements are all used to characterize the nickel oxide film, and the microbolometers and MIM devices that employ it.

The nickel film, when oxidized by exposure to oxygen plasma, is observed to only oxidize on the top surface. Nickel oxidized in a high temperature, dry O_2 environment is observed to undergo significantly higher oxidation, thereby making it more suitable for use in microbolometers and MIM devices. Resistivity mapping and profilometric thickness measurements provide a preliminary confirmation of more complete oxidation of nickel, and X-ray diffraction, and TEM/EDS analysis further confirms it. Ellipsometric measurements confirm that the thermally oxidized nickel oxide is highly absorptive in the infrared range of the spectrum, which is necessary for use in a microbolometer. Electrical

testing reveals that nickel oxide is indeed sensitive to incident infrared radiation, and shows a significant change in resistance upon its absorbance. The temperature coefficient of resistance calculated from electrical measurements is -0.23 %/°C. Testing of MIM devices reveals a new low-frequency resistive state switching mechanism that occurs due to a constant voltage bias being placed on the device. A theory of slow formation and destruction of thin conducting filaments is proposed to explain this behavior.

5.1 Future work

Future work can be done to further study these properties of nickel oxide. Now that a preliminary fabrication process and oxidation process is established, a specific designed experiment should be conducted to find the relationships between electrical results and device parameters such as nickel oxide thickness, which in this study, is the same for all devices. A number of process improvements can be made as well. Tantalum should not be used as the bottom electrode as it oxidizes easily under stress. A new oxidation-resistant electrode, such as a conductive oxide like indium-tin oxide (ITO), should be used for the bottom electrode. The nickel oxidation was conducted in a contaminated furnace tube, and the wafers were then disallowed from entering any plasma chamber, which prevented the dry etching of aluminum. Wet etching aluminum led to severe undercutting in critical areas. To solve this problem, a rapid thermal anneal process can be developed for nickel oxidation as this would remove the contamination issue, which would then allow the aluminum to be dry etched, thus making the entire

process CMOS compatible. Special care should also be taken to match the stresses of the various films so that adhesion problems do not present.

For the microbolometers, photoresist should not be used as the sacrificial bridge support film during nickel deposition, as it significantly hardens during the nickel deposition and patterning process, thus making it difficult to strip in a wet solvent strip. A hard mask that is easily stripped in wet chemistry and one that can survive a sputter deposition and lithography step should instead be used to make the air-bridge. Now that nickel oxide presents itself as a viable infrared absorptive film, controlled designed experiments should be conducted to maximize the TCR of the finished devices. The process variation should also be decreased to allow for the microbolometric arrays to function as imagers. The devices can be encapsulated to shield them from ambient light using a silicon cover. Their electrical response to a variety of infrared sources a should be investigated – such as a flame, human body, infrared LED's at various wavelengths, and so on – at different distances from the device. The incident infrared radiation can also be pulsed to see the frequency response. All these testing techniques would help further calibrate the sensitivity and characterize the performance of the microbolometers.

For the MIM devices, more device geometries should be designed to observe length and width effects on performance. A better bottom electrode metal would enhance the quality and repeatability of results obtained. Nickel oxide has shown definite resistive switching characteristics thus demonstrating its potential for use in resistive memory; however, the retention of the appropriate resistive states is an issue that requires more study in order

for nickel oxide to present itself as a ready candidate for resistive memory applications. Techniques involving in-situ mapping of current flow through the film stack during electrical testing can help solidify the theories for the resistive switching of nickel oxide.

This investigation of bolometric and resistive properties of nickel oxide lays the foundation for all the aforementioned future work. It demonstrates the potential of nickel oxide for serving as a multi-talented material for a variety of applications. Most significantly, this study successfully confirms the predicted oxidation kinetics at play during thermal oxidation of nickel.

References

[1] D. S. Kim et al., "The bolometric characteristic of thermally oxidized thin nickel film for an uncooled infrared image sensor," *Infrared Phys. & Tech.*, vol. 54, no. 1, pp. 10-12, 2010.

[2] Y. S. Lee et al., "Electric characteristic of nickel oxide film for the mirobolometer," *Proc. of SPIE*, vol. 8012, no. 80121P, 2011.

[3] Akhito Sawa, "Resistive switching in transition metal oxides," *Materials Today*, vol. 11, no. 6, pp. 28-36, June 2008.

[4] J. F. Gibbons and W. W. Beadle, "Switching properties of thin NiO films," *Solid-State Electronics*, vol. 7, no. 11, pp. 765-790, November 1964.

[5] T. H. Kim et al., "Resistance switching in polycrystalline NiOx thin film," in *2010 Conference on Optoelectronic and Microelectronic Materials and Devices (COMMAD)*, Canberra, 2010, pp. 223-224.

[6] D. C. Kim et al., "Electrical observations of filamentary conductions for the resistive memory switching in NiO films," *Applied Physics Letters*, vol. 88, no. 202102, 2006.

[7] R. T. Rajendra Kumar et al., "Room temperature deposited vanadium oxide thin films," *Materials Research Bulletin*, vol. 38, no. 7, pp. 1235-1240, 2003.

[8] H. Wang et al., "Low Temperature Fabrication of vanadium oxide films for uncooled bolometric detectors," *Infrared Physics Technology*, vol. 47, pp. 273-277, 2006.

[9] Shima Hisashi and Akinaga Hiroyuki, "Basics of RRAM based on transition metal oxides," in *International Symposium of Advanced Gate Stack Technology*, Albany, 2010.

[10] B. P. Andreasson et al., "Origin of oxygen vacancies in resistive switching memory devices," *Journal of Physics: Conference Series*, vol. 190, no. 012074, 2009.

[11] D. S. Kim et al., "Properties of reactively sputtered nickel oxide films as a microbolometric sensing material," *Proc. SPIE*, vol. 7660, no. 1B, 2010.

[12] N. Greenwood and A. Earnshaw, *Chemistry of the Elements*, 2nd ed. Oxford, UK: Butterworth-Heinemann, 1997.

[13] Lars Stixrude, Evgeny Waserman, and Ronald Cohen, "Composition and temperature of Earth's inner core," *Journal of Geophysical Research*, vol. 102, no. B11, pp. 24729–24740, November 1997.

[14] ReTi Metal. (2008) ReTi Metal Products. [Online]. http://www.retimetal.com/product-30-Nickel-sputtering-target.html

[15] National Institute of Standards and Technology. (2011) NIST Chemistry WebBook. [Online]. http://webbook.nist.gov/cgi/inchi/InChI%3D1S/Ni

[16] National Institute of Standards and Technology. (2011) NIST Chemistry WebBook. [Online]. http://webbook.nist.gov/cgi/cbook.cgi?ID=C78104

[17] K. Nomura. AIST ITSC Gallery. [Online]. http://staff.aist.go.jp/nomura-k/common/struc-coord/NiO-c.htm

[18] Vermont Safety Information Resources, Inc. (1997) SIRI MSDS Index. [Online]. http://hazard.com/msds/mf/baker/baker/files/n3060.htm

[19] R. Winston Revie, *Corrosion and Corrosion Control*, 4th ed. Hoboken, New Jersey, USA: John Wiley & Sons, 2008.

[20] Walter J. Moore and James K. Lee, "Kinetics of the Formation of Oxide Films on Nickel Foil," *Transactions of the Faraday Society*, vol. 48, pp. 916-920, March 1952.

[21] Thomas Grimsley. (2012, June) RIT SMFL Wiki. [Online]. https://wiki.smfl.rit.edu/

[22] Lynn Fuller. Dr. Lynn Fuller. [Online]. http://people.rit.edu/lffeee

[23] Peter Van Zant, *Microchip Fabrication*, 5th ed.: McGraw-Hill, 2000.

[24] Stanley Wolf and Richard N. Tauber, *Silicon Processing for the VLSI Era - Volume 1: Process Technology*.: Lattice Press, 2000.

[25] Richard C. Jaeger, *Introduction to Microelectronic Fabrication*.: Prentice Hall, 2002.

[26] Dan Fullerton, 0305-643 Thin Films Processes Lecture Notes, 2010.

[27] R. E. Pearson, 0305-201 Introduction to Microelectronics Lecture Notes, 2008.

[28] S. Zafar et al., "Measurement of oxygen diffusion in nanometer scale HfO2 gate dielectric films," *Applied Physics Letters*, vol. 98, no. 15, 2011.

[29] S. Zafar et al., "Resistance degradation in barium strontium titanate thin films," *Journal of Applied Physics*, vol. 86, no. 7, 1999.

[30] J. Goldstein et al., *Scanning Electron Microscopy and X-ray Microanalysis*.: Springer, 2007.

[31] H. F. Ounsi et al., "Quantitative and Qualitative Elemental Analysis of Different Nickel–Titanium Rotary Instruments by Using Scanning Electron Microscopy and Energy Dispersive Spectroscopy ," *Journal of Endodontics*, vol. 34, no. 1, pp. 53-55, January 2008.

[32] Scintag, Inc., *Chapter 7: Basics of X-ray Diffraction*. Cupertino, CA, USA, 1999.

[33] Jack Ord. Jack's Page: Basic Physics and Optics. [Online]. http://www.kw.igs.net/~jackord/ee/e7.html

[34] S. Sood et al., "Wet etching of sputtered tantalum thin films in NaOH and KOH based solutions," *Journal of Material Science: Materials in Electronics*, vol. 18, no. 5, pp. 535-539, 2006.

[35] A. A. Navid and A. M. Hodge, "Nanostructured alpha and beta tantalum formation - Relationship between plasma parameters and microstructure," *Materials Science and Engineering: A*, vol. 536, pp. 49-56, 2012.

[36] Edward McCafferty, *Introduction to Corrosion Science*.: Springer, 2010.

[37] M. L. Hoey et al., "rf plasma oxidation of Ni thin films sputter deposited to generate thin nickel oxide layers," *Applied Physics Letters*, vol. 97, no. 15, 2010.

[38] Pieter Kuiper. (2006) Wikipedia Public Domain.

[39] J. Jesper et. al, "Ellipsometry," Institute of Physics and Nanotechnology, Aalbord University, 2004.

[40] Salah A. Makhlouf, "Electrical properties of NiO films obtained by high-temperature oxidation of nickel ," *Thin Solid Films*, vol. 516, pp. 3112-3116, 2008.

Appendix

Fabrication Recipes

- **MOS RCA Bench – Standard RCA Clean**

1. APM dip – 10 minutes
    a) APM = 4500 ml H_2O + 300 ml NH_4OH + 900 ml H_2O_2
    b) Temperature = 75 °C
2. DI water rinse for 5 minutes
3. 50:1 HF dip – 1 minute
4. DI water rinse for 5 minutes
5. HMP dip – 10 minutes
    a) HPM = 4500 ml H_2O + 300 ml HCl + 900 ml H_2O_2
    b) Temperature = 75 °C
6. DI water rinse for 5 minutes
7. Spin/Rinse/Dry in SRD tool

- **SSI Track – Standard Coat recipe (10,000 Å photoresist film)**

1. Dehydration bake / HMDS priming
    a) HMDS vapor prime at 140 °C for 60 seconds
2. Spin coat: OiR-620 positive photoresist
    a) Dispense preset amount, then spin wafer at 3250 rpm for 30 seconds
3. Soft bake at 90 °C for 60 seconds

- **SSI Track – Metal Coat recipe (13,127 Å photoresist film)**

    1. Dehydration bake / HMDS priming
        a) HMDS vapor prime at 140 °C for 60 seconds
    2. Spin coat: OiR-620 positive photoresist
        a) Dispense preset amount, then spread at 400 rpm for 2 seconds
        b) Then spin wafer at 2000 rpm for 30 seconds
    3. Soft bake at 90 °C for 60 seconds

- **SSI Track – Standard Develop recipe**

    1. Post-exposure bake – 110 °C for 60 seconds
    2. Develop: CD-26 developer
        a) Wet surface of wafer with DI water
        b) Dispense developer, 50 second puddle, followed by 30 second rinse
        c) Spin dry at 3750 rpm for 30 seconds
    3. Hard bake at 140°C for 60 seconds

- **SSI Track – Metal Develop recipe**

    1. Post-exposure bake – 110 °C for 60 seconds
    2. Develop: CD-26 developer
        a) Wet surface of wafer with DI water
        b) Dispense 7 seconds, 68 second puddle, followed by 30 second rinse
        c) Spin dry at 3750 rpm for 30 seconds
    3. Hard bake at 140°C for 120 seconds

- **Drytek Quad, Chamber 3 – Silicon Etch, Recipe = ZEROETCH**

    1. 10 minute chamber season with dummy wafer
    2. Gas flows:
        a) 50 sccm CHF_3
        b) 25 sccm CF_4
        c) 10 sccm O_2
    3. RF Power = 200 W
    4. Pressure = 100 mTorr
    5. Time = 120 seconds

- **Solvent Strip – Standard Wet Photoresist Strip**

    1. Bath temperature = 75 °C
    2. 5 minute dip in left (dirtier) bath
    3. 5 minute dip in right (cleaner) bath
    4. 5 minute DI rinse
    5. Spin/Rinse/Dry in SRD tool

- **GaSonics Asher – Plasma O_2 Photoresist Strip (Recipe FF)**

    1. Gas Flows:
        a) 0.3 L/min Nitrogen
        b) 3.0 L/min Oxygen
    2. Pressure = 2.25 mTorr
    3. Total Process Time = 99 seconds
    4. High level lamp time (initial chamber heat up) = 15 seconds

5. Low level lamp time (maintains chamber temp) = 99 seconds
6. Repeat entire recipe.

- **Bruce Furnace Tube 1 – 5000 Å Pad Oxide Growth (Recipe 350)**

1. Boat out: Load wafers
2. Push in: Ramp to 800 °C, 10 L/minute N_2, 12 minutes
3. Stabilize: 800 °C, 10 L/minute N_2, 15 minutes
4. Ramp up: Ramp to 1000 °C, 5 L/minute N_2, 20 minutes
5. Flood: 1000 °C, 10 L/minute O_2, 5 minutes
6. Soak: 1000 °C, 3.6/2.0 L/minute O_2/H_2, 100 minutes
7. Anneal: 1000°C, 15 L/minute O_2, 5 minutes
8. Ramp down: Ramp down to 800 °C, 10 L/minute N_2, 40 minutes
9. Boat out: Unload wafers

- **Bruce Furnace Tube 8 – Nickel Oxidation (Recipe 20)**

1. (Manual) Boat out/Load wafers
2. Stabilize: 500 °C, 5 L/minute N_2, 35 minutes
3. Push in: Ramp to 500 °C, 5 L/minute N_2, 12 minutes
4. Stabilize: 500 °C, 5 L/minute N_2, 60 minutes
5. Soak: 500 °C, 15 L/minute O_2, 300 minutes
6. N2 Purge: 500 °C, 10 L/minute N_2, 5 minutes
7. Ramp down: Ramp down to 25 °C, 5 L/minute N_2, 35 minutes
8. Boat out: Unload wafers

- **CVC 601 – 2500 Å α-Ta Sputter**

1. Load wafers, and pumpdown to 10^{-7} Torr base pressure
2. Radiative heating: 20 min, 200 °C
3. Pre-sputter: 500 W, 5.5 mTorr, 43.6 sccm Ar + 16.3 sccm N_2, 5 min
4. TaN seed deposition: 175 W, 5.5 mTorr, 43.6 sccm Ar + 16.3 sccm N_2, 2 min
5. α-Ta deposition: 200 W, 5.5 mTorr, 43.6 sccm Ar, 30 min

- **PE 4400 – 2100 Å Ni Sputter**

1. Load wafers, and pumpdown to 10^{-7} Torr base pressure
2. Sputter Ni:
    a) Power = 400 W
    b) Gas flow = 40 sccm Ar
    c) Pressure = 5 mTorr
    d) Time = 60 min

- **PE 4400 – 7500 Å Al Sputter**

1. Load wafers, and pumpdown to 10^{-7} Torr base pressure
2. Sputter etch:
    a) Power = 500 W
    b) Gas flow = 40 sccm Ar
    c) Pressure = 5 mTorr
    d) Time = 20 min
3. Sputter Al:
    a) Power = 400 W

b) Gas flow = 40 sccm Ar

c) Pressure = 5 mTorr

d) Time = 125 min

- **LAM 490 – 2500 Å α-Ta Plasma Etch**

1. Gas Stabilize:

   a) Power = 0 W

   b) Pressure = 260 mTorr

   c) Gas = 200 sccm SF_6

   d) Time = 60 seconds

2. Etch:

   a) Power = 125 W

   b) Pressure = 260 mTorr

   c) Gas = 200 sccm SF_6

   d) Time = 150 seconds (for contact cut, time = 60 seconds)